Chapter 1
Single Nanomagnet Behaviour: Surface and Finite-Size Effects

Òscar Iglesias and Hamid Kachkachi

Abstract In this chapter we discuss some intrinsic features of nano-scaled magnetic systems, such as finite-size, boundary, shape and surface effects. We mainly review in a succinct manner the main results of previous works. We first present the basics of theoretical models and computational techniques and their applications to individual nanomagnets. Results of both simulations and analytic calculations for specific materials, compositions and shapes are given based on these models.

1.1 Introduction

Nanomagnetism is the magnetism of nano-scaled objects. In general, the magnetic state of a body is characterized by its macroscopic property that is magnetization, which is the module of the statistical average of the magnetic moment vector, projected onto the applied field. The module and orientation of the latter are stable with respect to thermal fluctuations during a certain interval of time that depends on the underlying material, the size and shape of the magnetic body, as well as external environment parameters such as temperature and magnetic fields. Depending on the system's setup, the magnetic moment may adopt several possible orientations corresponding to the various minima of its energy, which are separated from each other by energy barriers that depend in turn on various intrinsic physical parameters of the system as well as on external ones. In bulk systems the energy barriers happen to be too high for the system to cross them (within the observation time) and to spontaneously switch from one state to another. On the opposite, in nano-scaled systems these barriers are drastically reduced leading to rather short switching times. Indeed, when the size of the system reduces from bulk to nanometric scales, the magnetic

---

Ò. Iglesias (✉)
UB and IN2UB, Barcelona, Spain
e-mail: oscariglesias@ub.edu

H. Kachkachi
UPVD and PROMES CNRS UPR8521, Perpignan, France
e-mail: hamid.kachkachi@promes.cnrs.fr

D. Peddis et al. (eds.), *New Trends in Nanoparticle Magnetism*,
Springer Series in Materials Science 308,
https://doi.org/10.1007/978-3-030-60473-8_1

properties are drastically modified owing to the fact that finite-size, boundary and surface effects then play a major role. Roughly, finite-size and boundary effects are due to the nanometric size and shape of the system, while surface effects emerge from the symmetry breaking of the crystal structure at the boundaries of the nano-object. As such, before addressing the study of nano-scaled magnetic systems, call them *nanomagnets* (NM), we ought to distinguish between these effects and try to assess their separate contributions, at least from the standpoint of theory. In reality all these effects are intertwined together and it is not possible to single out the impact of each effect on the macroscopic observable, for the simple reason that the surface is intimately connected with boundary, shape and size.

Accordingly, in this short review we will attempt to cover, with no pretension to be exhaustive, the main results of previous works on these effects. We first recall a simple comparison and clear distinction between finite-size, boundary and surface effects. Next, we will proceed through chosen examples to illustrate each one of these effects on the main physical observables which are relevant in the context of nanomagnetism [1]. We will then consider the magnetization reversal, relaxation time and blocking temperature and the (quasi-)equilibrium properties of the NMs such as the hysteresis loop, the "critical temperature", spin configuration and, of course, the magnetization itself. We will also discuss, where necessary, the main computing methods (analytical and numerical) employed.

1.1.1 Finite-Size Versus Boundary Effects

As discussed above, when dealing with confined magnetic systems, such as a NM, one should distinguish, at least from a theoretical point of view, between finite-size, boundary, and surface effects. For instance, for a cube with simple cubic (sc) lattice (see Fig. 1.1 left) with periodic boundary conditions (pbc), there is only one environment (crystal field) with coordination number $z = 6$.

In this case, the temperature behavior of the magnetization is marked by the well-known $M \sim 1/\sqrt{\mathcal{N}}$ tail in the critical region, where $\mathcal{N}$ is the total number of spins in the NM (Fig. 1.1, right). In the case of more realistic free boundary conditions (fbc), a cube with sc structure shows four different environments with $z = 3, 4, 5, 6$ (see Fig. 1.2 left). In this case, in addition to the previous finite-size effects, one is faced with boundary effects. These induce stronger fluctuations that suppress the magnetization of the system (see Fig. 1.2 right). Considering both cases of pbc and fbc allows for a separate estimation of the related effects. Now, if the boundary of a system with fbc is endowed with a surface anisotropy, which is indeed a consequence of boundary defects, we may then speak of surface effects, in addition to the finite-size and boundary effects (see below).

For both pbc and fbc, it can be shown [2] that the magnetization can be written in a simple form. At low temperature and zero field, M (when normalized) deviates from unity, its saturation value, according to

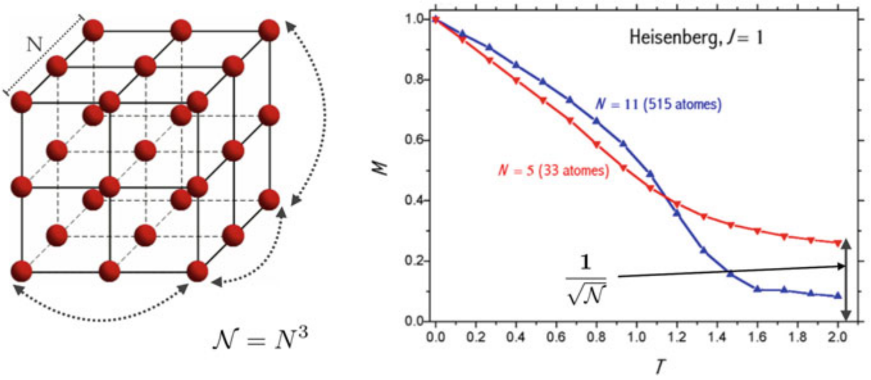

Fig. 1.1 Cubic system with pbc and thermal behavior of the magnetization for two sizes

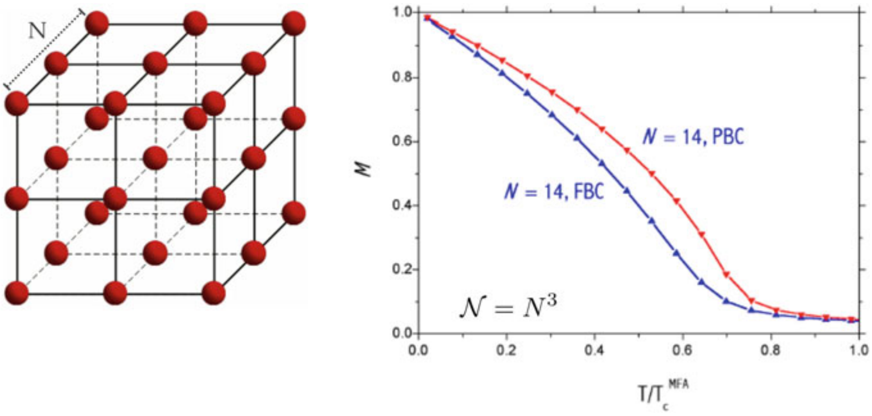

Fig. 1.2 Cubic system with fbc and thermal behavior of the magnetization for pbc and fbc systems

$$M \cong 1 - \frac{\theta}{2} W_N, \tag{1.1}$$

where

$$W_N = \frac{1}{\mathcal{N}} {\sum_{\mathbf{k}}}' \frac{1}{1 - \lambda_{\mathbf{k}}}, \theta = \frac{T}{T_{\mathrm{c}}^{\mathrm{MFA}}} \tag{1.2}$$

and for a three-dimensional ($d = 3$) sc lattice $\lambda_{\mathbf{k}} = (\cos k_x + \cos k_y + \cos k_z)/d$. It is important to note that W_N in (1.2) for pbc and fbc differ only by the definition of the discrete wave vectors [2, 3], since

$$k_\alpha = \begin{cases} 2\pi n_\alpha / N, & \text{pbc} \\ \pi n_\alpha / N, & \text{fbc} \end{cases}, \qquad n_\alpha = 0, 1, \ldots, N - 1 \tag{1.3}$$

where $\alpha = x, y, z$. This subtle difference is responsible for much stronger thermal fluctuations in the fbc model due to boundary effects. Indeed, the separation between two successive values of the wavenumber k for fbc is smaller than that for pbc. Therefore, more spin-wave modes are excited in the fbc system, thus leading to a weaker magnetization.

Surface Effects

Surface effects are due to the breaking of crystal-field symmetry at the boundary of the NM, and in reality they cannot be disentangled from boundary effects. In order to study surface effects one has to resort to microscopic theories capable of distinguishing between different atomic environments and taking account of physical parameters such as single-site surface anisotropy, exchange and dipolar interactions (DI), in addition of course to the magneto-crystalline anisotropy and magnetic field. Unfortunately, this leads to complex many-body problems which can only be efficiently dealt with, in general, using numerical approaches such as Monte Carlo simulations or numerical solutions of the Landau-Lifshitz equation (see Sect. 1.2.2).

Shape Effects

Apart from the finite-size, boundary and surface effects, the NM shape is also a distinctive property that has an influence not only on its magnetic properties but also on the optical, plasmonic and electric properties of nanostructured systems. The equilibrium states and hysteresis loops are clearly dependent on the NM's shape (see Sect. 1.3.2). Indeed, when the shape changes, the distribution of atomic spins changes and the core-to-surface ratio is thereby modified, leading to a change in the corresponding effective fields. There is even a drastic change in the distribution of local fields that lead to new spin configurations and thereby to new magnetic states with different macroscopic properties.

1.2 Basic Theoretical Models and Computing Tools

Building theoretical models for confined magnetic systems requires explicitly taking into account the local atomic environment with all its specificities which are strongly dependent on the size, shape and underlying material. On the other hand, the model have to account for the macroscopic behavior of the net magnetic moment which is rather sensitive to the external stimili such as heat and magnetic fields. Such a behavior is exemplified by *superparamagnetism*, which is a fast shuttling motion of the net magnetic moment between its energy minima. Low temperature magnetic order within the NM has to incorporate exchange coupling between the magnetic ions, the Zeeman coupling to the external field and the (local) magnetic anisotropy energy. Apart from this, the spatial lattice in which the magnetic ions reside has to reflect the real crystallographic structure of the material to be studied, since lattice geometry may play an essential role in establishing the minimum energy configurations by inducing competing orders and frustration. For these reasons, a reasonable model and the corresponding Hamiltonian must necessarily make use of the atomic magnetic moment as its elementary building block. Consequently, the techniques for computing the various physical observables using such a Hamiltonian, generally borrowed from bulk systems, have to be adapted and extended to such nano-scaled systems, namely spin-wave theory, relaxation time theories, and Monte Carlo simulations, just to cite a few. In some limit, depending on the set of physical parameters, it is possible to investigate the magnetization reversal of a NM within an assembly using a macroscopic model which represents the NM through its net magnetic moment. Obviously, this model ignores any internal features of the NM and focuses on its global behaviour in an external magnetic field and/or in contact with a heat bath. There are several variants of such a model but all of them may be considered as extensions of the initial Stoner-Wohlfarth (SW) and/or the Néel-Brown (NB) models [4–10]. Up to scaling factors, these models are all *one-spin problems* and will then be referred to as OSP. On the other hand, *many-spin problems* which involve the atomic spins of the NM will be referred to as MSP. In this section we shall first succinctly present the macroscopic model (OSP) and the well known results they render for the magnetic moment of a NM under the usual conditions of temperature and magnetic field. Next, we will turn to the presentation of the MSP approach, the corresponding Hamiltonian and computational methods. In the subsequent sections, we will present the main results of the application of this approach to a NM, regarded as a many-spin crystal with its specific features.

1.2.1 Macrospin Approach

As discussed earlier, in the framework of the macroscopic model (OSP), one concentrates on the behaviour of the net magnetic moment, ignoring any (local) process that leads to its onset. Thus, the exchange energy becomes a constant and plays no role in the minimization of the total energy. Consequently, the Hamiltonian only includes the anisotropy and Zeeman energies, namely

$$\mathscr{H} = -\frac{KV}{M^2}(\mathbf{M}.\mathbf{e})^2 - (g\mu_B)\,\mathbf{H}\cdot\mathbf{M}, \tag{1.4}$$

where K is an effective uniaxial anisotropy constant, $\mathbf{e}$ the verse of its easy direction and V the volume of the NM. Upon writing $\mathbf{M} = M\mathbf{s}$, $\mathbf{H} = H\mathbf{e}_h$ and introducing the dimensionless anisotropy and field parameters

$$\sigma = \frac{KV}{k_B T}, \quad h = \frac{(g\mu_B)\,HM}{2KV}, \tag{1.5}$$

the energy in (1.4), measured with respect to thermal energy $k_\mathrm{B}T$, becomes

$$-\beta\mathscr{H} = \sigma\left[(\mathbf{s}\cdot\mathbf{e})^2 + 2h\mathbf{s}\cdot\mathbf{e}_h\right]. \tag{1.6}$$

T is the absolute temperature and k_B the Boltzmann constant $\beta \equiv 1/k_\mathrm{B}T$.

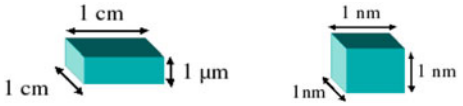

Fig. 1.3 A bulk system versus a nanoscale one. *Source* Reprinted with permission from [1]. Copyright (2020), Elsevier Books

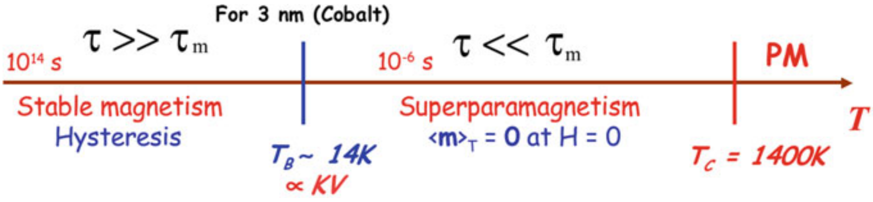

Fig. 1.4 Temperature axis

1.2.1.1 Relevant Time, Length and Energy Scales

To a first approximation, the (dimensionless) anisotropy-energy barrier in zero field is given by σ. For comparison, in Fig. 1.3 we evaluate the latter for two blocks of a given material, one of "bulk" dimensions (cm), on the left, and the other on the right with dimensions of the order of a nanometer.

To be more specific we consider cobalt for the underlying material at room temperature, $T = 300\,\mathrm{K}$, in the absence of a DC magnetic field. We find for the energy barrier $\sigma = \frac{KV}{k_B T} \sim 10^{15}$. This leads to a switching time between the two minima which is given by $\tau \propto e^{\sigma} \sim \exp\left(10^{15}\right)$. On the other hand, for the cluster on the right $\sigma \sim 10^{-2}$ and $\tau \sim 10^{-10}$ s. This implies that as the magnet's size is reduced to the nanometer scale, the switching of the macroscopic magnetic moment between the various energy minima becomes possible at room temperature. In fact, even at much lower temperatures this switching becomes accessible to experiments. This fundamental new effect (i.e. superparamagnetism), induces a shift in the relevant temperature scale. Indeed, as depicted in Fig. 1.4, in nano-scaled systems the most relevant temperature is that which corresponds to the thermal energy that is sufficient for overcoming the energy barrier, rather than the Curie temperature, as is relevant for bulk systems. This new temperature is known as the *blocking temperature* and is denoted by T_B. In fact, its should be called the unblocking temperature because it is the temperature above which the magnetic moment climbs up the energy barrier and switches its orientation.[1]

In general, the energy barrier may be lowered by various mechanisms and/or different external stimuli:

---

[1] More precisely, for magnetic measurements with measuring time $\tau_m \sim 100$s (such is the case in magnetometry measurements), the superparamagnetic range is $0 \leq \Delta E/k_B T < \ln(\tau_m/\tau_0) \simeq 25$.

- At zero temperature, an applied static magnetic field h reduces the energy barrier as follows $\Delta E = \sigma\,(1-h)^2$. When h reaches a critical value h_c (here 1), the energy barrier is entirely suppressed and the magnetic moment of the system switches to the new available minimum. This hysteretic switching mechanism is well described by the so-called Stoner-Wohlfarth model [4, 8].
- At finite temperature, and even at zero magnetic field, the switching probability of the magnetic moment becomes nonzero owing to thermal fluctuations. Such a stochastic mechanism is well described by the so-called Néel-Brown model [5, 7, 9, 11]. Alongside the well-known work of Néel, Brown, and also that of Aharoni (1969), there is a fundamental approach developed by Langer (1967–69) for multivariate systems [12–15]. The only limitation of Langer's approach is that it applies to situations where the extrema of the energy potential are well defined in the sense that they are not flat. Indeed, this approach is based on the quadratic expansion of the energy potential at the various extrema (minima, maxima and saddle points). In practice, this turns out to be applicable to intermediate-to-high damping regimes.

For practical applications, such as information storage, one seeks to increase the storage density by using rather small magnetic elements. However, reducing the volume of these elements leads to rather low energy barriers and thereby to large switching rates, especially at room temperature. This drastically deteriorates the temporal stability of the information stored in the media. One way out consists in considering magnetic materials with large anisotropy constants K (as in CoPt), but then the critical field h_c required to suppress the energy barrier, which corresponds to writing a new information, becomes too large and inaccessible to nano-scaled devices. This is what we could call the *superparamagnetic tri-lemma*. Consequently, the nanomagnetism community sought for other alternatives while keeping in mind the two main objectives for practical applications, namely large storage densities and long temporal stability at room temperature. Two of such alternatives have been suggested: (i) add a time-dependent field on top of the static magnetic field [16–21], thus assisting the switching process without having to entirely suppress the energy barrier, and (ii) apply a laser beam to the system so as to locally reduce the anisotropy contribution. This is what it is called *heat-assisted magnetization reversal* (HAMR) mechanism.

1.2.2 Many-Spin Approach

In NMs of a diameter of the order of 10 nm (e.g. of cobalt), a great number of atoms is located on the outer shell. Now, we know that the latter undergoes lattice reconstructions and atomic rearrangements which in turn lead to a crystal-field symmetry breaking inducing strong local inhomogeneities. The consequence of this is *nonuniform atomic spin configurations*. For instance, as the surface anisotropy increases in intensity, the switching mechanism becomes less coherent and rather operates cluster-wise, leading to steps in the hysteresis loop and the limit-of-metastability

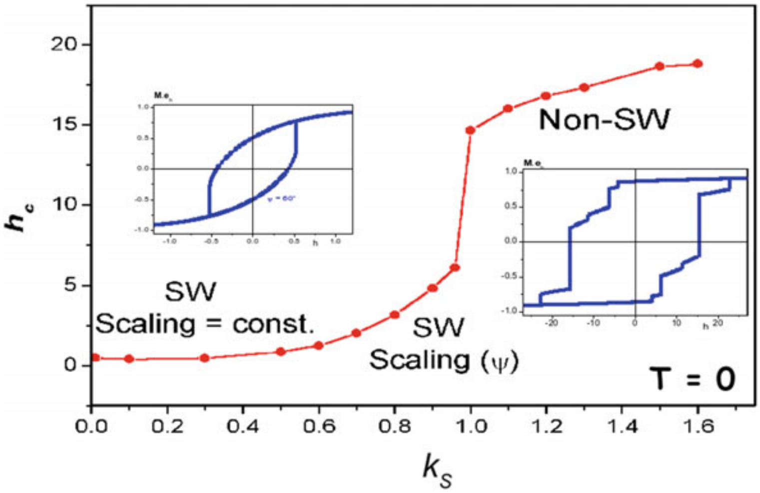

Fig. 1.5 Effects of surface anisotropy on the hysteresis loop and validity of the macrospin approach ($k_S \equiv K_S/J$). *Source* Reprinted with permission from [1]. Copyright (2020), Elsevier Books

curve can no longer be scaled with the Stoner-Wohlfarth astroid [22]. The situation can be summarized in Fig. 1.5, where the Stoner-Wohlfarth switching field is plotted against the ratio of surface anisotropy constant to exchange coupling ($k_S \equiv K_S/J$).

1.2.2.1 Hamiltonian

In order to account for and investigate the effect of spin noncolinearities, one has to resort to microscopic approaches that necessarily involve the atomic magnetic moment with continuous degrees of freedom as their building block. Such approaches then take account of the local environment inside the system, including the microscopic interactions and single-site anisotropy. Consequently, this amounts to adopting many-spin approaches in which the NM is considered as a crystal of $\mathscr{N}$ atomic magnetic moments $\boldsymbol{m}_i = (g\mu_B S)\, \boldsymbol{s}_i$, where $\mathbf{s}_i$ is the atomic unit spin vector ($\| \mathbf{s}_i \| = 1$) on site i. The interaction of these atomic moments is usually described with the help of the (classical) anisotropic Dirac-Heisenberg model [22]

$$\mathscr{H} = -\sum_{\langle i,j \rangle} J_{ij} \mathbf{s}_i \cdot \mathbf{s}_j + \mathscr{H}_Z + \mathscr{H}_{an}, \tag{1.7}$$

where J_{ij} is the exchange coupling which may be ferromagnetic or antiferromagnetic and whose nominal value depends on the nature of the link $i \leftrightarrow j$. So we may have a different coupling for core-core (J_{cc}), core-surface (J_{cs}) and surface-surface (J_{ss}) links.[2]

Next,

$$\mathscr{H}_Z = -(g\mu_B)\mathbf{H} \cdot \sum_{i=1}^{\mathscr{N}} \mathbf{s}_i \tag{1.8}$$

is the Zeeman energy of interaction of the external magnetic field **H** with all atomic magnetic moments $\boldsymbol{m}_i$. Finally, $\mathscr{H}_{an}$ in (1.7) is the (uniaxial) single-site anisotropy energy

$$\mathscr{H}_{an} = -\sum_i K_i (\mathbf{s}_i \cdot \mathbf{e}_i)^2, \tag{1.9}$$

with easy axis $\mathbf{e}_i$ and constant $K_i > 0$. If the site i is located in the core, the anisotropy axis $\mathbf{e}_i$ is taken along some reference z axis and $K_i = K_c$. In fact, K_c is the effective anisotropy constant and $\mathbf{e}_i$ is the easy axis of the effective anisotropy that is usually assumed to include the NM's shape anisotropy. For NMs grown out of a magnetic material with cubic anisotropy, the term $\mathscr{H}_{an}$ may also comprise a cubic contribution. Altogether, in the absence of experimental data, the anisotropy constant K_c and easy direction are often assumed to be the same as those of the underlying bulk material. For surface spins, the anisotropy is also considered as uniaxial with a constant $K_i = K_s$ and an easy axis that is taken along the radial direction (i.e., transverse to the cluster surface), as illustrated in Fig. 1.6. Several works have also considered the same model with $K_i < 0$, i.e. with an easy axis that is tangential to the surface.

A more physically plausible model of surface anisotropy was introduced by Néel [6] with

$$\mathscr{H}_{an} = \frac{K_s}{2} \sum_i \sum_{j=1}^{z_i} (\mathbf{s}_i \cdot \mathbf{u}_{ij})^2, \tag{1.10}$$

where z_i is the coordination number of site i and $\mathbf{u}_{ij} = \mathbf{r}_{ij}/r_{ij}$ the unit vector connecting the site i to its nearest neighbors (see Fig. 1.7). This model sounds more realistic because the anisotropy at a given site occurs only when the latter loses some of its neighbors, e.g. when it is located at the boundary.

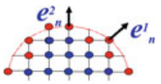

Fig. 1.6 Transverse Surface Anisotropy model. *Source* Reprinted with permission from [1]. Copyright (2020), Elsevier Books

---

[2] We define the core as the group of atomic spins whose coordination number z is equal to that of the bulk material (= 6 for a sc lattive and 12 for an fcc lattice). The other spins with lower z are considered as surface spins.

1.2.2.2 Weak Surface Effects

The study of the dynamics of NMs in the many-spin approach, along what was discussed in Sect. 1.2.1, presents tremendous difficulties related with the analysis of the energyscape (minima, maxima and saddle points), which is a crucial step in the calculation of relaxation rates and investigation of the magnetization reversal at finite temperatures. One may then address the question as to whether it is possible to establish some conditions under which one may adopt a (simpler) macroscopic approach and avail oneself from the corresponding full-fledged theory of magnetization dynamics. An answer to this question was provided in [23, 24] in the case of not-too-strong surface effects, i.e. when the surface anisotropy is not strong enough so as to consider the spin configuration as almost collinear (see Fig. 1.8).

Under this condition an *effective macroscopic model* was built for the net magnetic moment of the NM evolving in an effective energy potential. The latter turns out to be an infinite polynomial in the components of this macroscopic magnetic moment [23–26]. However, the 2nd- and the 4th-order terms are the leading contributions to the effective energy and the corresponding coefficients depend, both in magnitude and sign, on the underlying material, the size and shape of the NM, and the microscopic parameters (coupling, anisotropy, etc.) [26]. In the absence of a magnetic field, we then have the effective energy [23–26]

$$\mathscr{E}_{\text{eff.}} = -K_2 m_z^2 + K_4(m_x^4 + m_y^4 + m_z^4). \tag{1.11}$$

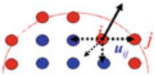

Fig. 1.7 Néel Surface Anisotropy model. *Source* Reprinted with permission from [1]. Copyright (2020), Elsevier Books

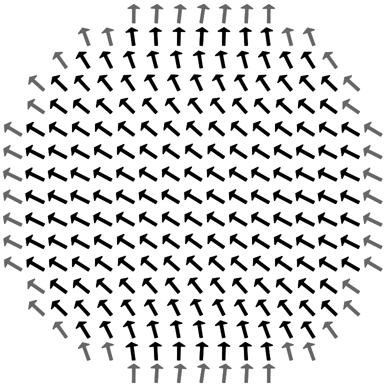

Fig. 1.8 Spin configuration of the middle plane of a spherical NM with relatively weak surface anisotropy and a net magnetic moment along the diagonal. *Source* Reprinted with permission from [1]. Copyright (2020), Elsevier Books

The coefficient K_2 of the second-order[3] contribution is in fact the result of two contributions, one stemming from the initial core uniaxial anisotropy and a new contribution that is induced by surface anisotropy (see below). The latter contribution is much smaller than the former because its coefficient contains the product $(K_c/J)(K_s^2/J) \ll 1$. The 4th-order coefficient K_4 in (1.11) was expressed in terms of the microscopic parameters as [23]

$$K_4^{(0)} = \kappa_2^{(0)} \frac{\mathscr{N} K_s^2}{zJ}, \tag{1.12}$$

where K_s, z, J are respectively the on-site surface anisotropy constant (transverse or Néel), the coordination number, and the exchange coupling of the many-spin NM. $\kappa_2^{(0)}$ is a surface integral that depends on the underlying lattice, the shape, and the size of the NM and also on the surface-anisotropy model. For instance, for a spherical NM (of ~ 1500 spins) cut from a simple cubic lattice with Néel's surface anisotropy, $\kappa_2^{(0)} \simeq 0.53465$.

To sum up, this effective macroscopic model provides us with an intermediate approach that: (i) involves a macroscopic magnetic moment whose dynamics is much easier to study since its potential energy is a function of only two variables, and (ii) does inherit the intrinsic features of the NM through the microscopic physical parameters entering the coefficients of the effective potential.

1.2.2.3 Validity of the Effective Models

The effective model (1.11) comes in as a handy tool for investigating the dynamics of the magnetization of NMs in a macroscopic approach that still captures some of the intrinsic features of the NMs [27, 28], see Sect. 1.3.1.1. However, it is not an easy matter to validate this model in experiments. The main reason is that the quartic term in (1.11) is a pure surface contribution that appears even in the absence of core anisotropy (see [23, 24]) and which may renormalize the cubic anisotropy of the (underlying) magnetic material the NM might be made of. Hence, it is not obvious how to disentangle this surface-induced 4th-order contribution from the intrinsic cubic anisotropy of magnetic materials. Nonetheless, at least for thin disks where the effective anisotropy is mostly of (boundary) surface origin, this quartic contribution may become dominant. An example of this situation was provided by cobalt nano-dots with enhanced edge magnetic anisotropy [29].

Obviously, for rather weak surface anisotropy the cubic contribution drops and the Stoner-Wohlfarth model is reinstated as a good approximation to the many-spin NM. Some experimental macroscopic estimates of the surface anisotropy constant yield, e.g. for cobalt $K_s/J \simeq 0.1$ [30], for iron $K_s/J \simeq 0.06$ [31], and for maghemite NMs $K_s/J \simeq 0.04$ [32]. However, one should not forget that this effective constant depends on the NM's size, among other parameters such as the material composition.

---

[3] With respect to the power of the components of the net magnetic moment.

Moreover, for a NM of diameter 2 nm, we may expect higher anisotropies. For such materials, the effective macroscopic model has been shown to be valid for $K_s/J \leq 0.25$ in a simple cubic lattice and $K_s/J \leq 0.35$ in a face-centred cubic lattice [26].

In Sect. 1.3.1.1 we discuss the effect of surface anisotropy on the relaxation rate in a study that has been made possible with the help of this effective model.

In the case of an assembly of magnetic NMs this model was used to compute the magnetization, the static susceptibility and the ac susceptibility. More precisely, the system studied is an ensemble of macrospins, each described with the help of the effective macroscopic model, and mutually interacting via the long-ranged dipolar coupling. In such a setup, it was possible to investigate the competition between (intrinsic) surface effects and dipolar interactions [28, 33–35] and to provide (semi-)analytical expressions for the observables mentioned above taking account of temperature, applied DC field, surface anisotropy and dipolar interactions. It is clear that such analytical developments would not be possible for an assembly of NMs treated as many-spin systems.

1.2.2.4 Strong Surface Anisotropy

When the conditions discussed above are not met, one has to deal with the Hamiltonian in (1.7) in its full generality with respect to the various energy contributions.

Thus, as discussed earlier, all techniques, both analytical and numerical, that are usually applied to bulk systems for investigating the magnetic properties, have to be adapted to nano-scaled systems. In particular, spin-wave theory, which is the study of the fluctuations of local spins, has to be extended so as to include the fluctuations of the net magnetic moment as well. This has been done in [2, 3] and references therein. The choice of the computing method depends on the observable of interest and on the approach considered. For equilibrium properties, the hysteresis loop and the switching field, for instance, is computed by numerically solving the deterministic Landau-Lifshitz equation without the Gaussian field. Within the macrospin approach, this equation is in fact a system of two (three) coupled equations in the system of spherical (Cartesian) coordinates, whereas within the many-spin approach this leads to a system of $2\mathscr{N}$ $(3\mathscr{N})$ coupled equations. However, in all cases the numerical procedure is quite straightforward and uses standard routines such as the Euler, Heun or Runge-Kutta methods [36, 37]. General magnetic properties of a many-spin system with, in principle, an arbitrary set of physical parameters, are also accessible to Monte Carlo simulations.

The classical Monte Carlo (MC) method based on the Metropolis algorithm is a standard technique [38] used in principle to simulate equilibrium statistical properties taking averages over a sample of possible spin configurations. At difference from atomistic simulations based on the Landau-Lifshitz equations, which are well suited for dynamic studies because they give the time evolution of magnetic moments, in MC simulations they are evolved through a sequence of MC steps with no real correspondence to real time. Even so, attempts have been made to establish a time quantification of MC steps in some particular cases [39, 40] showing that this simulation technique can also be used to qualitatively understand dynamic magnetization processes such as magnetic relaxation or hysteresis. In brief, at each MC step, one selects a single spin from the lattice either randomly or sequentially and a change of its orientation is proposed, repeating the sequence a number of times equal to the total number of spins. At each selection, a new trial orientation of the spin, the corresponding energy change ΔE and Boltzmann probability $p(\Delta E, T) = \exp(-\Delta E/K_B T)$ are computed. Then the new spin orientation is accepted if either $\Delta E < 0$ or $p(\Delta E, T) > r$ [$r \in (0, 1)$ being a uniform random number], otherwise the trial is rejected and the initial spin orientation is kept. For Ising spins, there is one option to change the sign of the spin variable with probability $1/2$, but for Heisenberg spins, the new trial step can be chosen in different ways as long as detailed balance condition is met. Instead of using as trial moves random directions on a sphere, it turns out to be more convenient to perform trials inside a cone around the current spin direction whose aperture can be tuned, in order to keep a high trial acceptance rate [41–43]. It has been noticed that it is of crucial importance to use a combination of methods (random, inside a cone and spin flip) when simulating NM with inhomogeneous properties such as surface anisotropy or NM with core/shell structure (see Sects. 1.3.2.1 and 1.3.2.3).

In order to account for the superparamagnetic behavior of the NM net magnetic moment the MC method was extended in [3] by including global rotations of the net magnetic moment, in addition to the usual (local) rotations of the atomic spin. The semi-analytical expressions for the magnetisation in terms of temperature and magnetic field were derived it was shown that there are three field regimes separated by two critical values of the magnetic field, namely the one that suppresses the global rotation and the higher one that suppresses spin waves.

The dynamics of a many-spin NM can in principle be tackled by solving the set of coupled (stochastic) Landau-Lifshitz equations written for atomic spins [44, 45]. Indeed, solving the (stochastic) Landau-Lifshitz equation with a Langevin (thermal) field is a very versatile technique that can deal with multi-variate systems and is thus well suited for investigating equilibrium and dynamic behavior of such many-spin systems. However, this method inherently includes time consuming subroutines that are necessary for (i) generating sequences of arrays of stochastic numbers and (ii) computing averages over sufficiently large ensembles of time spin trajectories. The other technique would consists in solving the Fokker-Planck equation but this requires writing a hierarchy of equations that depend on the energy potential. This means that this procedure is somewhat model-dependent. Moreover, this technique is limited in practice to a small number of degrees of freedom, since otherwise this hierarchy becomes too cumbersome to write and rather costly to solve numerically. As such, and as far as NMs are concerned, this technique has been applied to a maximum of two coupled magnetic moments [46]. In conclusion, the study of the dynamics of NMs in the many-spin approach can only be done efficiently using the Landau-Lifshitz equation, even though this remains a tremendous numerical task.

1.3 Results

In the following sections we shall present a sample of our previous results on finite-size, boundary, shape and surface effects. We first present results for model NMs with a simple cubic lattice, spherical and cubic shapes. Next, we discuss the results for more specific situations with antiferromagnetic couplings and core/shell configurations.

1.3.1 Finite-Size Effects

1.3.1.1 Switching Field

For many-spin NMs of variable size, but which still exhibit a collinear spin configuration, the hysteresis loop can be scaled with that rendered by the macrospin Stoner-Wohlfarth model, even in the general case of a field applied at an arbitrary angle with respect to the core easy axis.

The effect of finite-size on the hysteretic properties of NMs have been investigated by many authors, see [36, 37, 47] and references therein.

In Fig. 1.9 we plot on the left the coercive field of a spherical NM and on the right the Stoner-Wohlfarth astroid. We see that the results for a many-spin NM with physical parameters within the range of the OSP model scale with those of the Stoner-Wohlfarth model. The scaling constant is the ratio of the number of core spins to

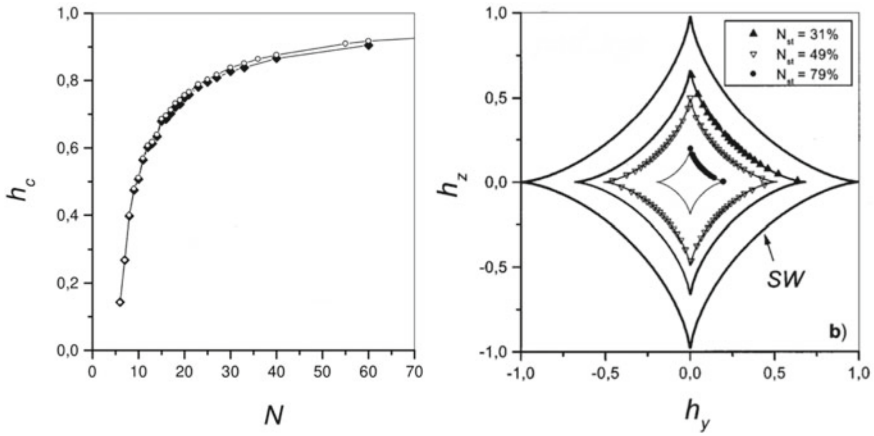

Fig. 1.9 Left: coercive field versus the linear size of a spherical NM. Right: Switching field of a spherical NM with $ks/j \simeq 0.01$, for different values of the surface-to-volume ratio $N_{st} = N_s/\mathcal{N}$. Calculations performed using the Landau-Lifshitz equation. *Source* Reprinted with permission from [37]. Copyright (2020), AIP Publishing LLC

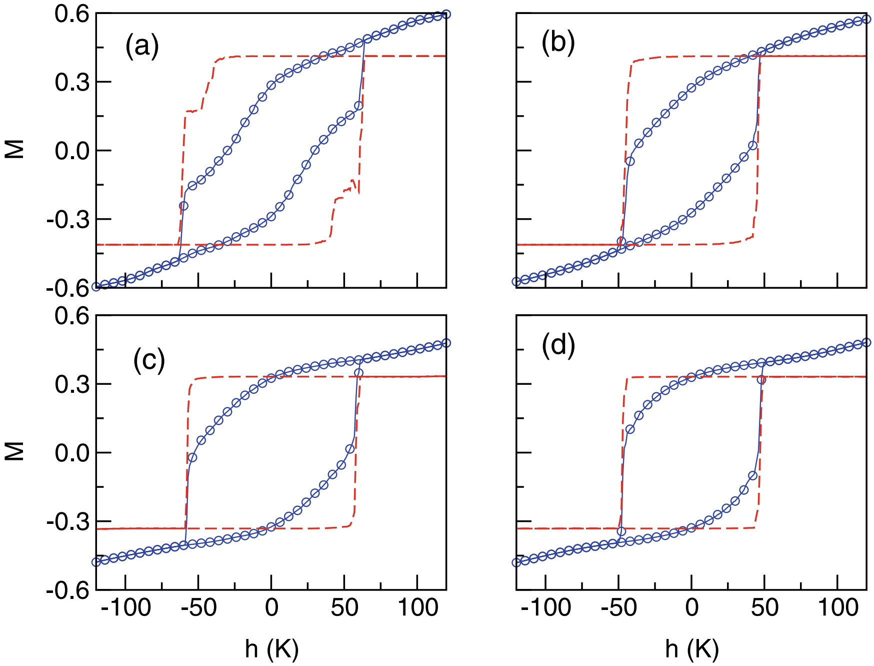

Fig. 1.10 Surface (continuous line) and core (dashed line) contributions to the hysteresis loop for NM of diameters $D = 3\mathrm{a}$, $T = 10$ K (**a**); $D = 3\mathrm{a}$, $T = 20$ K (**b**); $D = 6\mathrm{a}$, $T = 10$ K (**c**); $D = 6\mathrm{a}$, $T = 20$ K (**d**). Adapted from [48] Copyright 2020 American Physical Society

that of the NM's total number of spins. Moreover, the limit-of-metastability curves (astroids) for all sizes fall inside the Stoner-Wohlfarth astroid. This means that when boundary and surface effects, and the spin noncollinearities they entail, are ignored the magnetic properties of the NM can be described with the help of the macrospin model (or OSP).

Next, we consider the case of infinite uniaxial anisotropy thus restricting the orientation of the magnetic moments to that of Ising model. The reason for this choice is to study in pure form the effect of finite-size without interference from surface anisotropy effects. As a particular example with important applications, we consider a ferrimagnetic oxide such as maghemite. In this kind of oxides, Fe ions reside on a spinel structure where the spins have different coordination and antiferromagnetic couplings depending on the sublattice (tetra and octahedral) they belong to. The Ising variables interact through exchange interactions that may vary in value and sign from atom to atom depending on the spatial arrangement of the nearest neighbours [48, 49]. Since not all magnetic interactions can be fulfilled, and in spite of the collinear alignment of the spins, intrinsic geometrical frustration exists that is in part responsible for some of the peculiar properties of this kind of NM.

Then, in Fig. 1.10 we show hysteresis loops at different temperatures for NM with diameters $D = 3$a, 6a. First of all, we note that the saturation field and the high-field susceptibility increase as the NM size is reduced, since these quantities are mainly associated with the progressive alignment of the surface spins towards the field direction. Thus, the loops of the smallest NM resemble those found in ferrimagnetic NM [50–52] and other bulk systems with disorder [53, 54], increasing their squaredness (associated with the reversal of M as a whole) with the size. In fact, by plotting separately the contributions of the core and the surface to the total magnetization (see Fig. 1.10, dashed lines), we see that the loop of the core is almost perfectly squared independently of temperature and NM size, indicating a reversal of its magnetization with a well-defined ferrimagnetic moment. Instead, the loop of the surface reveals a progressive reversal of M, which is a typical feature associated to disordered or frustrated systems [53]. Nonetheless, for a wide range of temperatures and NM sizes, it is the reversal of the surface spins that triggers the reversal of the core. This is indicated by the fact that the coercive field of the core is slightly higher but very similar that of the surface. At zero temperature it was shown in [37] that the surface switches before the core in spherical NM with moderate surface anisotropy.

1.3.1.2 Magnetization Thermal Behaviour

In Fig. 1.11 we show the magnetization of a (model) spherical NM as a function of the reduced temperature. This is the ratio of temperature T to the critical temperature (T_{PBC}) of the cube-shaped NM with size of 40^3 and periodic boundary conditions. The corresponding magnetization is denoted M_{PBC}. This is compared with the magnetization of the core of a spherical NM of variable size and total number of spins $\mathcal{N} = 909, 3766, 6330$, with a surface contribution of 53%, 41%, 26%, respectively. For the details of the system and computing method see [55].

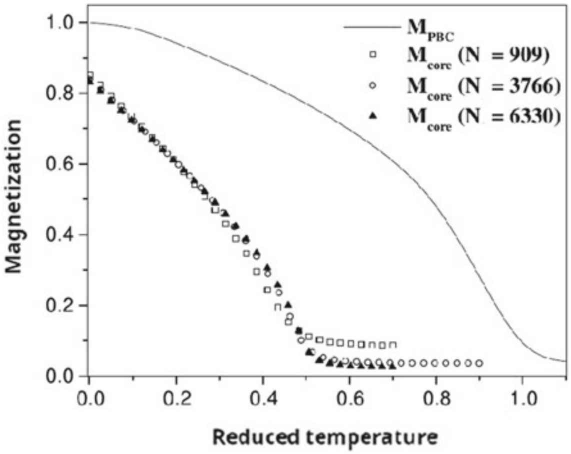

Fig. 1.11 Magnetization as a function of (reduced) temperature. Calculations performed using Monte Carlo simulations. *Source* Reprinted with permission from [56]. Copyright (2020), Springer

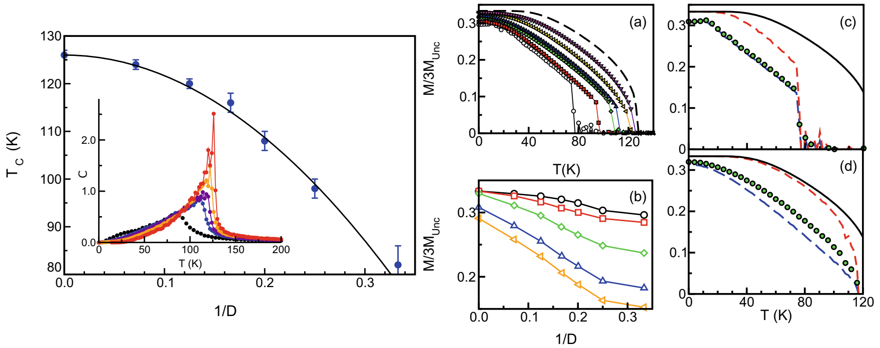

Fig. 1.12 Left panel: NM size dependence of the transition temperature T_c from paramagnetic to ferrimagnetic phases for spherical maghemite NM with fbc. The displayed values have been obtained from the maximum in the specific heat. The continuous line is a fit to (1.13) Inset: Thermal dependence of the specific heat for the same sizes as in the main panel. Right panel (**a**) shows the thermal dependence of the magnetization M obtained by progressive cooling from high T at a constant rate, $\delta T = -2$ K starting from a random configuration of spins, for NM of diameters $D = 3$a, 4a, 6a, 8a, 10a, 14a (symbols) and pbc conditions, in a system of linear size $N = 14$ (dashed line). In panels (**c**) and (**d**) the contributions of the surface (blue dashed line) and core spins (red dashed line) have been distinguished from the total magnetization (circles) for NM with diameters $D = 3$a, 8a. The results for pbc conditions, in a system of linear size $N = 14$, have also been included for comparison (continuous line). Panel (**b**) displays the size dependence of M_{Total} at different temperatures 10, 20, 40, 60, 70 K from upper to lowermost curves. Adapted from [48] Copyright 2020 American Physical Society

It is clearly seen that the critical temperature and magnetization are dramatically reduced in the core of the NM. The reduction of the critical temperature is obviously due to the finite-size. There is a size-dependent reduction of the critical temperature by up to 50% for the smallest NM. The same result has been found by Hendriksen et al. [60] and many other authors.

Next, we discuss finite-size effects in some specific systems. Accordingly, for maghemite NM, and as a first example of purely finite-size effects on equilibrium properties, we present results of the ordering temperature dependence on the NM size for diameters varying between 3 and 14 unit cells (corresponding to real NM sizes of 2.5–12 nm) as extracted from the peak in the thermal dependence of the specific heat that signals a second-order transition from a paramagnetic to a ferrimagnetic order. In Fig. 1.12, we can see that T_C decreases with decreasing NM size, approaching the bulk value extracted from a simulation performed using pbc on a system with linear size $N = 14$. The obtained dependence can be fitted accurately to the predictions of finite-size scaling theory [57, 58] to a scaling law of the kind

$$\frac{T_c(\infty) - T_c(D)}{T_c(\infty)} = \left(\frac{D}{D_0}\right)^{-1/\nu}. \tag{1.13}$$

This expression fits nicely the MC data with $D_0 = (1.86 \pm 0.03)$a being a microscopic length scale (in this case, it is roughly twice the cell parameter), and a critical exponent $\nu = 0.49 \pm 0.03$, which seems to indicate a mean field behaviour [59]. This result can be ascribed to the high coordination of the O and T sublattices. The fitted curve is drawn in Fig. 1.12 where deviations from scaling are appreciable for the smallest diameters, for which corrections to the finite-size scaling in (1.13) may be important [57]. Thus, these results discard any important surface effects on the ordering temperature and are consistent with spin-wave calculations [60] and old MC simulations [61]. Similar finite-size effects have been found in fine NM [62] of $MnFe0_4$, but with a surprising increase of $T_c(D)$ as D decreases, which has been attributed to surface effects due to the interactions with the NM coating. More recently, other experimental [63–68] and theoretical [69–72] studies have reported similar scaling laws, although with different values of the scaling exponents depending on the NM composition and spin lattice.

The effects of the NM size can also be appreciated in the thermal dependence of the magnetization of an individual NM when going from the high temperature paramagnetic phase through T_C, the ordering temperature. Finite-size effects show up as changes in the $M(T)$ law with NM size D as compared to bulk behavior. To study the effects of a free surface and of finite size on the magnetization of the NM, we compare in Fig. 1.12a the results for four NM diameters ($D =$ 3a, 4a, 6a, 8a, 10a, 14a, symbols) with those corresponding to $N = 14$ with pbc (representing the behavior of the bulk). The main feature observed is the reduction of the total magnetization M_{Total} with respect to the pbc case (continuous line) due to the lower coordination of the spins at the surface, which hinders ferrimagnetic order at finite temperatures. Figure 1.12c, d clearly show the role played by the surface (blue dashes) and the core (red dashes) in establishing the magnetic order. On one hand, independently of the NM size, the core tends to a perfect ferrimagnetic order at low T (marked by $M = 1/3$), progressively departing from the bulk behavior as T approaches T_c, this finite-size effect being more important as the NM size decreases. However, the surface magnetization does not reach perfect ferrimagnetic order at $T = 0$ even for $D = 8$ due to the reduced coordination of the spins. For this reason, a rapid thermal demagnetization is observed leading to M_{Surf} that significantly departs from the bulk behavior.

It is worthwhile to note that for all the diameters studied, there is a temperature range in which this demagnetization process is linear, this range being wider as the NM size decreases. In this linear regime, the NM demagnetization becomes dominated by surface effects since the core and surface behaviors are strongly correlated. Linear demagnetization is indicative of the effective 3D-2D dimensional reduction of the surface shell and has previously been observed in thin film systems [73, 74] and in simulations of rough FM surfaces [75]. M_{Total} is always strongly dominated by the surface contribution, progressively tending to the bulk behavior as the NM size is increased.

In Fig. 1.12b, we show the size dependence of the M_{Total} at different temperatures. All the curves follow a quasi-linear behavior with $1/D$ except for very small NM sizes ($D = 3$). This is consistent with the existence of a surface layer of constant thickness Δr independent of D and with reduced magnetization with respect to the core. With these assumptions, the size dependence of M can be expressed as

$$M(D) = M_{\text{Core}} - \Delta M \frac{\Delta r S}{V} = M_{\text{Core}} - \Delta M \frac{6\Delta r}{D}, \tag{1.14}$$

where S and V are the surface and volume of the NM, and $\Delta M = M_{\text{Core}} - M_{\text{Surface}}$.

1.3.2 Effects of Shape and Surface Anisotropy

Recent advances in the synthesis methods and characterization techniques in the field of nanomagnetism have allowed us to have control on the production of NM with specific shapes and morphologies. It has been demonstrated that magnetic nanoparticles can be synthesized with precise control over their sizes, shapes, compositions, and structures [76–79]. In particular, the control of their shape can be used to tailor functional properties for specific biomedical and technological applications [80, 81]. In what follows, we will first present examples that illustrate how shape is related to distinct magnetic properties of NM and then will continue presenting three phenomena that illustrate how the existence of surface anisotropy and interfaces affect the magnetic properties of NM.

1.3.2.1 Effects of Shape in the Reversal of Oxide NPs

As a first example, let us consider two maghemite NM with spherical and cubic shape and similar radius and length of 20 nm, as the ones used in an experimental study of the heating properties relevant to hyperthermia applications [82]. Analyzing the hysteresis loops simulated by atomistic MC (see Fig. 1.13), we see that their shape and area undergo a substantial change just for the fact of changing their shape, since they have the same (real) values of the core and surface anisotropies. In particular, notice that the loop area of the cubic NM is larger than that of the spherical one. It has been checked that this is accomplished independently of the NM size, thus pointing to a genuine shape effect associated with changes occuring at the surface of the NM. Note that the difference in areas stems from qualitative loop shape differences around the coercive and closure field points that can be traced back to the different reversal processes of the surface spins as clearly observed on in the right panel of Fig. 1.13. Since the loop area is directly related to the specific absorption rate, these simulation results give a convincing explanation of experiments that show a systematic superior magnetic heating efficiency of cube-shaped NM as compared to spherical ones of similar sizes [82–87].

In our next example, we compare the phenomenology of spherical and ellipsoidal NM [88, 89]. Notice that, in contrast with the previous sections, the values of the

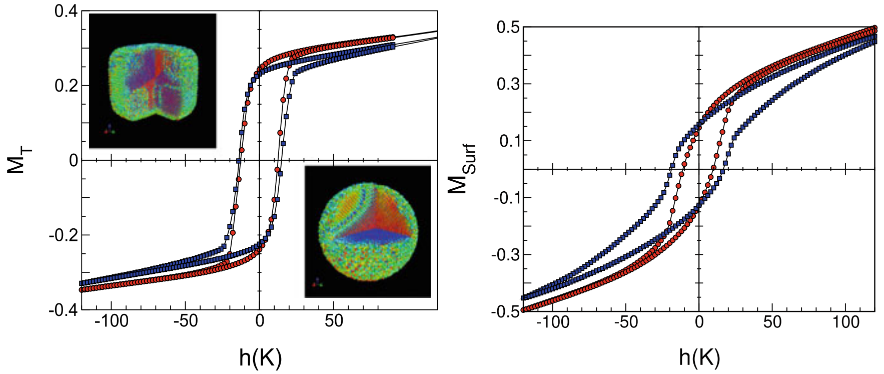

Fig. 1.13 Left panel: Hysteresis loop for a spherical (red circles, diameter 20 nm) and a cubic NM (blue squares, side 20 nm) obtained from MC simulations of an atomistic spin model of maghemite at low temperature. In both, uniaxial anisotropy at the core and Néel surface anisotropy have been considered. Snapshots show the spin configurations at the positive coercive field. Spins have been colored according to their projection onto the magnetic field direction (z axis) from red (+1) to blue (−1). Right panel: Contribution of the surface spins only to the hysteresis loop of a spherical (red circles) and a cubic NM (blue squares)

anisotropy constants here are given in temperature units and that they correspond to maghemite (see Sect. 1.3.2.2 for details).

By comparing, in Fig. 1.14, the loops for $k_S = 10$ to those for $k_S = 100$, we see that the coercive field increases and the remanence decreases with increasing surface anisotropy, independently of the elongation L of the NM. Moreover, the presence of disordered groups of spins at the surface, induced by surface anisotropy, makes the loops more elongated and increases the closure fields of the loops as found also in experiments on ferrimagnetic oxides [90]. The rounding of the loops near the coercive field clearly indicates a progressive departure from a uniform reversal mechanism with increasing k_S. When looking only at the M_z component, not much difference is appreciated between the loops for NM with different L because of the compensation of the spin components transverse to the field direction due to the symmetry of revolution of the NM around the z axis. However, upon further inspection of the ${M_n}^{\mathrm{Surf}}$ and M_n^{Core} contributions and animated snapshots taken along the loops [91], the details of the reversal process can be better understood.

We first note that when k_S is increased from $k_S^\star$ the reversal mechanism changes from quasi-uniform (induced by the core) rotation at low k_S values, to a process in which the formation of surface hedgehog-like structures induce the non-uniform switching of the whole NM. In the first regime ($k_S = 10$ case in Fig. 1.14), the core and surface spins point mostly along the z axis ($M_n^{\mathrm{Core}} \approx 1$, $M_n^{\mathrm{Surf}} \ll 1$) except near the coercive field where they make short excursions towards the radial direction driven by the surface anisotropy (see the dips in M_n^{Core} and the cusps in ${M_n}^{\mathrm{Surf}}$). However, for $k_S > k_S^\star$ ($k_S = 100$ case in Fig. 1.14), the surface spins remain near the local radial easy-directions ${M_n}^{\mathrm{Surf}} \approx 1$) during the reversal, while the core spins

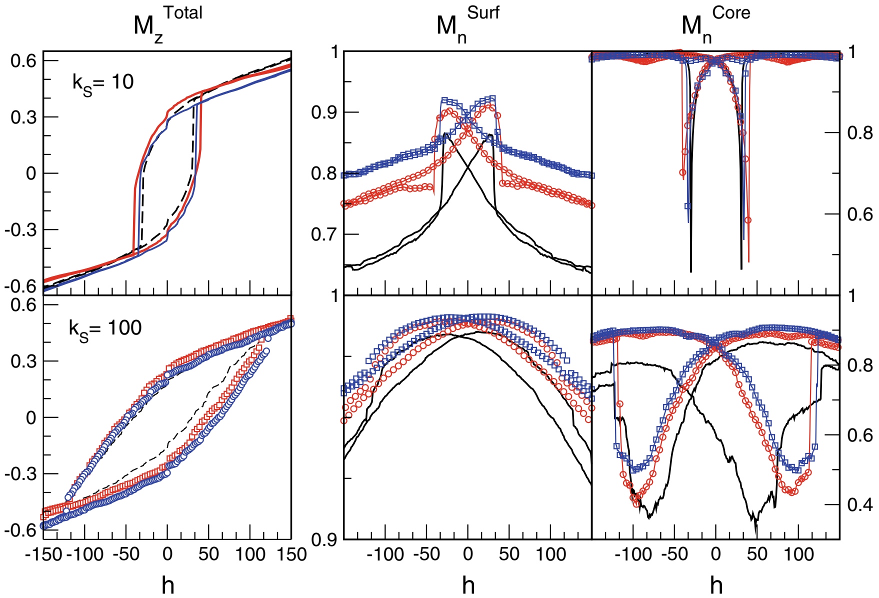

Fig. 1.14 Hysteresis loops for maghemite ellipsoidal NM with two values of the radial surface anisotropy constant $k_S = 10, 100$. Black lines are for a spherical NM with diameter $D = 3$, symbols are for an ellipsoidal NM with $D = 3$ and $L = 6$ (circles), 8 (squares). Left panels display the total magnetization while central and right panels show the surface and core contributions to M_n. Reprinted from [88] Copyright (2004), with permission from Wiley-VCH

are dragged away from the z local easy-axis by the surface spins during the reversal, except for values of h near the closure field. This is indicated by the widening of the dips in M_n^{Core} and the global decrease of M_n^{Core} values as k_S increases. Finally, let us remark also that, for all the k_S considered, the ${M_n}^{\mathrm{Surf}}$ values along the whole hysteresis loops increase with increasing L, which indicates that the surface spins remain closer to the local radial direction during the reversal as the NM become more elongated. Upon increasing L, the dips in M_n^{Core} become less profound for $k_S > k_S^{\star}$, an indication that reversal of core spins along the radial direction is suppressed by the elongation. However, for weak anisotropy ($k_S < k_S^{\star}$), the more elongated the NM are, the greater the deviation of surface spins towards the radial direction during the reversal.

1.3.2.2 Surface Effects on the Thermal Dependence and Hysteresis of Oxide NP

In order to study surface effects in atomistic simulations, it is necessary to account for the three dimensional character of the atomic spins considering them as Heisenberg classical spins ($\mathbf{s}_i$) that can point in any direction in space (see (1.7)). Moreover, apart from the exchange interaction, it is necessary to include magnetocrystalline anisotropy and to introduce the distinct surface Néel anisotropy term (1.10) for spins close to the surface with reduced coordination as compared to bulk. While the values of bulk anisotropy constants K_C can be obtained indirectly by magnetic measurements, the surface contribution K_S is more difficult to evaluate. However, for maghemite with $K_C \simeq 4.7 \times 10^4$ erg/cm^3 [92, 93], K_S has been estimated as $K_S \simeq 0.06$ erg/cm^2 from Mössbauer experiments [94, 95]. Therefore, in the simulations for maghemite NM, we will vary the core anisotropy values in the range $k_C = 0.01 - 1$ K and those of the surface anisotropy in the range $k_S = 1 - 100$ K.

We start again by examining the thermal dependence of the magnetization for different diameters, now with a variable k_S and fixed $k_C = 1K$. For small surface anisotropy ($k_S < 10$), the demagnetizing process has a linear dependence with T over a wide range of temperature for all NM sizes studied. This linear dependence is similar to that found for the model with Ising spins [96] in Sect. 1.3.1.2 . However, in that case, the linear dependence was blurred as the NM size increased and it was limited to a narrower range of temperatures. For Heisenberg spins, instead, this behavior is clearly observed for all the simulated D's and extends up to the ordering temperature, being more evident for the largest NM and for the core spins (see Fig. 1.15). This linear behavior is in agreement with the variation predicted by a surface spin wave theory and, therefore, is indicative of the effective 2D behavior of the surface shell, that completely dominates the magnetic behavior of the NM [97]. This is also in contrast with the results for FM NM (not shown, [98]) where, due to the absence of frustration, the core contribution dominates as indicated by a clear downward curvature of the $M(T)$ curves [98, 99]. Note also that the ordering temperature, marked by appearance of a non-zero M_z value, increases with the NM size as in the Ising model, but its value is lower.

Next, we focus on the magnetic order reached after the cooling process. For the real maghemite NM, the attained configurations are the result of the competition between

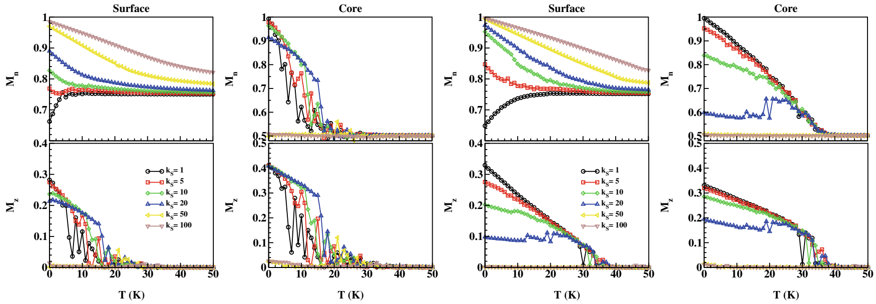

Fig. 1.15 Spherical NM ($D = 3$a for left panels and $D = 6$a right panels) with the real maghemite AF interactions. Thermal dependence of the surface (left column) and core (right column) contributions to M_z and to M_n during a progressive cooling from a high T at a constant rate $\delta T = -1$ K. Different curves correspond to different values of the surface anisotropy $k_S = 1, 5, 10, 20, 50, 100$ with $k_C = 1$. Reprinted from [100] Copyright (2004), with permission from Elsevier

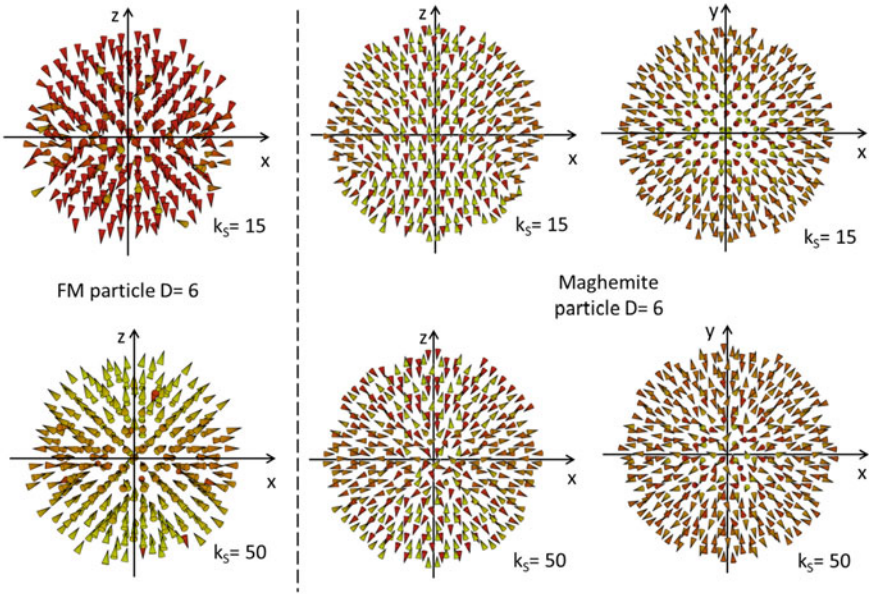

Fig. 1.16 Snapshots of the equilibrium configurations attained after cooling from a high temperature disordered state for FM (left column) and ferrimagnetic maghemite spherical (central and left columns) NMs with $D = 6a$ and maghemite lattice structure. Configurations are shown for two values of the surface anisotropy constant $k_S = 15$ and $k_S = 50$. The pictures display the central unit cell corresponding to a cut through an equatorial plane along the Z or XY axes

the frustration caused by the intra and intersublattice AF coupling of the spins and the distribution of local anisotropy directions at the surface. As a consequence, due to the dominant AF intersublattice coupling, a greater degree of disorder at the surface is induced with respect to the FM case [98]. For low k_S values ($k_S \lesssim 20$ curves in Fig. 1.15), the NM orders into a quasi-AF state in which spins in each sublattice are almost aligned along the core easy-axis, the states attained at $T = 0$ have core spins ordered in an AF state along the z-axis but surface spins that progressively depart from perfect alignment along the core easy-axis direction as k_S is increased. This is indicated by the approach of M_n towards 1 for core spins and towards 0.5 for surface spins as T is reduced (see the upper panels in Fig. 1.15). Note that while for the FM NM the maximum value of the total magnetization M_z is 1, this is not the case for the real maghemite NM since now the low T value of the total magnetization is given essentially by the contribution of noncompensated spins [96] (see Fig. 1.15).

With increasing k_S, this quasi-AF kind of ordering changes. $M_n^{\text{Surf}} \to 1$ at low T (see the upper panels in Fig. 1.15), which indicates that surface spins start to depart from the core easy-axis towards the local radial direction. Moreover, $M_n^{\text{Core}} \to 0.5$, a clear signature that the radial deviation of surface spins drive the core spins progressively towards the radial direction as k_S is increased. As a consequence throttled structures as those seen for $k_S = 15$, $D = 6$ in Fig. 1.16 start to form (similar results

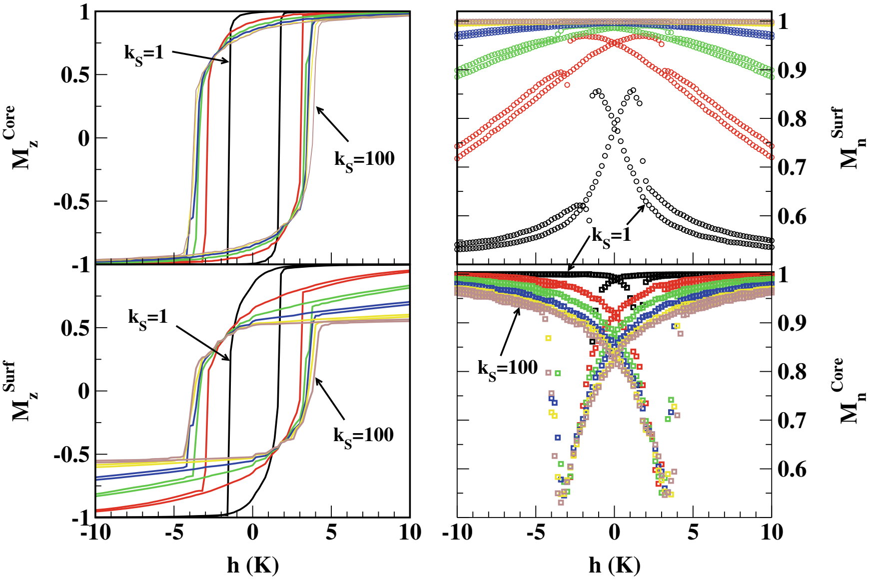

Fig. 1.17 Hysteresis loops for a spherical NM of diameter $D = 3a$ with FM interactions. The core anisotropy constant is $k_C = 1$, the results for several values of the surface anisotropy constant are displayed $k_S = 1, 5, 10, 20, 50, 100$. The magnetization component along the applied field direction is shown in lower right panel, the core contribution is displayed in the upper right panel. Right panels show the surface and core contributions to M_n, the sum of spin projections onto the local anisotropy axis. Reprinted from [100] Copyright (2004), with permission from Elsevier

have been found for other lattices and compositions in [71, 101–104]). Finally, for k_S above a critical value, $k_S^\star$, hedgehog-like configurations are favoured by the dominant radial anisotropy contribution (see for example the configuration for $k_S = 50$, $D = 6$ in Fig. 1.16). The direct visualization of equilibrium configurations presented in Fig. 1.16 shows that the reduction of the saturation magnetization with NM size observed experimentally in different fine NM of ferrimagnetic oxides, can be attributed to the random canting of surface spins caused by the competing AF interactions between sublattices [50, 105]. Moreover, as the results of our simulations confirm, the degree of disorder at the surface is larger than for the FM NM due to the complex interplay between the AF intralattice interactions and the local anisotropy easy-axes.

Next, we continue analyzing the influence of surface anisotropy on the reversal processes. First, we consider the results for a FM NM with the same lattice structure than maghemite shown in Fig. 1.17 for different values of k_S. For a FM NM, the hysteresis loops are dominated by the surface contribution for all values of k_S studied as indicated by the non-squaredness of the loops around the coercive field. For high values of the surface anisotropy ($k_S = 50, 100$), a magnetic field as high as $h = 20$ K is able to saturate the core, but the surface spins instead point along the radial direction during the magnetization process. This is more clearly reflected on the right panels of Fig. 1.17, where we see that for high k_S, M_n remains close to 1 at the

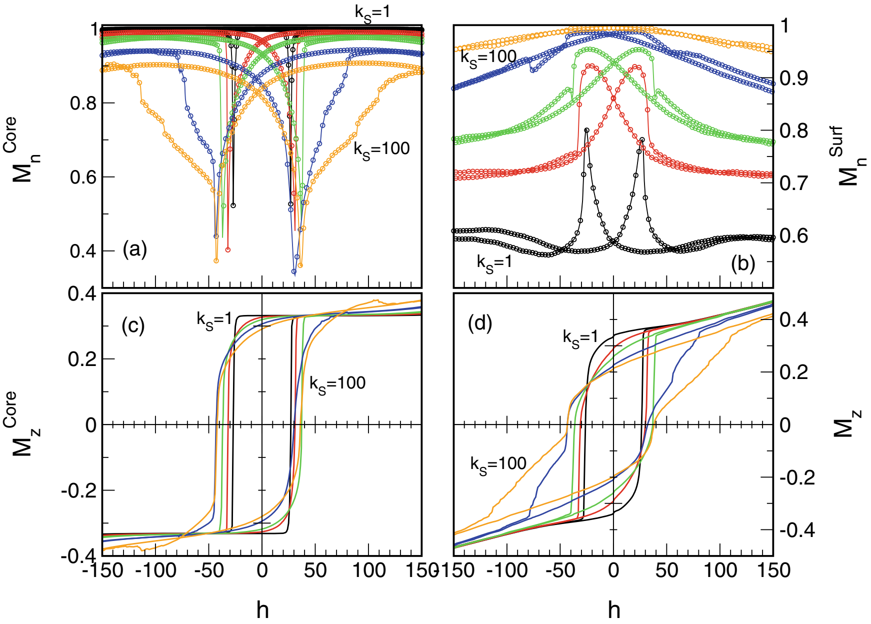

Fig. 1.18 Hysteresis loops for a real maghemite spherical NM with diameter $D = 6a$ for different values of the surface anisotropy constant $k_S = 1, 10, 20, 50, 100$. The different panels show the (**a**) core and (**b**) surface contributions to the projected magnetization along the local anisotropy axes (M_n), (**c**) the core contribution to the component of the magnetization along the field direction, and (**d**) the total magnetization

surface during all the reversal process, while the core spins depart from their easy directions ($M_n \sim 1$) dragged by the surface towards the radial direction close to the coercive field, where $M_n \sim 0.5$.

The hysteresis loops for the FM NM are to be compared with those for real ferrimagnetic maghemite NM presented in Fig. 1.18 for $D = 3a$, $6a$ and k_S ranging from 1 to 100. Although the reversal process is still dominated by the surface spins, notice that now the loops for the ferrimagnetic NM become more elongated and have higher closure fields than those for the FM NM of the same size, indicating the frustrating character of the interactions in ferrimagnetic oxide NMs [106]. Moreover, a reduction in the high field susceptibility and an increase of the closure fields is also observed. These features are due to the dominance of surface anisotropy over exchange interactions that create surface disordered states which become more difficult to reverse by the magnetic field.

More importantly, there is a change in the magnetization reversal mechanism upon increasing k_S above $k_S^{\star}$, the value for which a change in the low T configurations was observed. For $k_S < k_S\star$ (see Fig. 1.18), the core and the surface have similar h_C and closure fields. The NM core reverses in a quasi-uniform manner with the spins pointing mostly along the z-axis ($M_n \approx 1$) except near h_c, and with the surface

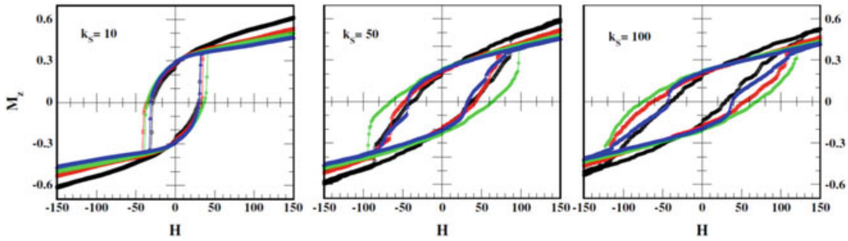

Fig. 1.19 Hysteresis loops of maghemite particles with diameters $D = 3a$ (black),$D = 4a$ (blue),$D = 5a$ (red),$D = 6a$ (green). Each panel corresponds to a different value of k_S as indicated

spins following the core reversal (with $M_n < 1$ indicating alignment close to the z direction) [107]. However, at higher k_S (see Fig. 1.18 for $k_S > k_S^\star$), surface spins remain close to the local radial direction ($M_n \approx 1$) during all the reversal process, driving the core spins away from their local easy axis and making their reversal non-uniform ($0.5 < M_n < 1$) due to the appearance of the hedgehog-like structures during the reversal [107]. Notice also that for $k_S > k_S^\star$ a series of steps in the hysteresis loops along the irreversibility line can be observed as also seen in [108]. Each step corresponds to the jump of a cluster of surface spins that are able to overcome the energy barrier induced by the high radial anisotropy at that field.

The influence of NM size on the hysteresis loop at $T = 0$ depends on the range of values of k_S, although some features are common to all of them, as can be seen in Fig. 1.19. As the NM size increases, the high field susceptibility decreases while the loops at different D all cross at $h = 0$. However, for k_S values below the critical one ($k_S < k_S^\star$), h_C is almost size independent, although the coercive field for the core spins of NM with high anisotropy is higher for the smaller NM. In contrast, for $k_S > k_S^\star$ (see the panels with $k_S = 50, 100$ in Fig. 1.19) h_C increases with increasing NM size except for the $D = 6$ NM. These results are in qualitative agreement with those reported by Morales et al. [109] for maghemite NMs with sizes ranging between 3 and 14 nm. They observed a slight increase of the coercive field with decreasing size for the range of sizes reported here.

1.3.2.3 Core-Shell NPs

For many technological applications, it has been shown to be useful to synthesize NP with non-homogenous materials having, for example, a gradient in composition when going from the inner to outer parts [110] or having a core and shell made of materials with different magnetic properties [111]. The last case is somehow unavoidable since most magnetic elements are easily oxidized when exposed to air or aqueous media. These NP can be otherwise produced by controlled chemical synthesis [112, 113] in a variety of morphologies and compositions. Magnetic core/shell nanoparticles with

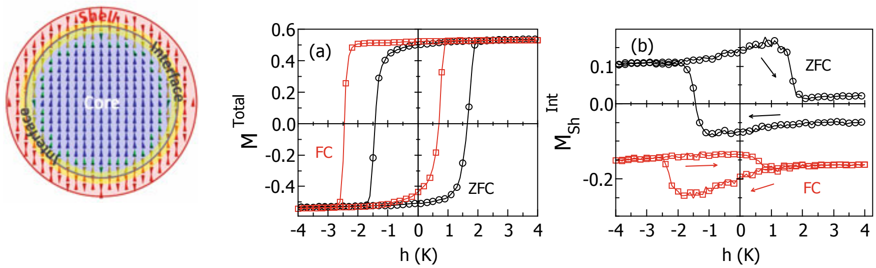

Fig. 1.20 Left: schematic drawing of model of a core/shell NM of total radius R used in the MC simulations. The spins sit on the nodes of a sc lattice. The AF shell has width R_{Sh} (red and yellow spins) and the FM core (blue and green spins) a radius $R_C = R - R_{Sh}$. The core/shell interface (green and yellow spins) is formed by the core (shell) spins having nearest neighbours on the shell (core). Right: Hysteresis loops for a core/shell NP with radius $R = 12\,a$ obtained from a ZFC state and after FC down to $T = 0.1$ in a field h_{FC} for $J_{\mathrm{Sh}} = -0.5 J_{\mathrm{C}}$ Panel (**a**) displays the total normalized magnetization component along the field direction. Panel (**b**) shows the normalized contributions of the shell spins at core/shell interface to the total magnetization of the loop. Adapted from [124] Copyright (2020) American Physical Society

functionalyzed shells and coatings are also necessary in biomedicine for applications in targeted delivery and diagnostics [81, 114–116].

An attractive composition results from the combination of a FM or AF core surrounded by an AF or FM shell (usually an oxide) coupled by the exchange interaction at the interface between them. Interesting proximity effects result from the structural modification and competition of different magnetic orderings at the FM/AFM interfaces [117–123]. In particular, the so-called exchange bias (EB) phenomenon which, in brief, consists in the shift of the hysteresis loop along the field axis after cooling the sample from high temperature through the Néel temperature of the AF, in the presence of a magnetic field [121]. For thin film FM/AF layers, different semi-analytical models (for a review see [121] and references therein) based on the macrospin approach have been proposed to account for the values of the observed EB fields, but none of them applies to NM, where the role played by the interface needs to be understood at an atomistic level. In order to unveil the microscopic origin of all the phenomenology associated to EB effects in NM, a minimum model that captures the main ingredients of a single NM with core/shell structure can be developed as depicted by the drawing shown in Fig. 1.20.

For simplicity, a core/shell NM is made of atomic spins placed on the nodes of a sc lattice inside a sphere of radius R (measured in multiples of the unit cell dimensions a) and inside which three regions are distinguished: core with radius R_C, shell of thickness $R_{Sh} = R - R_C$ and interface formed by the core (shell) spins having nearest neighbors on the shell (core). To account for the finite values of anisotropy in real systems, we consider Heisenberg spins interacting through the Hamiltonian of (1.7) with uniaxial anisotropy as in Fig. 1.6. Core/shell structures are typically made of a FM core and AF shell [121, 124–126], represented by $J_{\mathrm{C,Sh}} \lessgtr 0$ exchange constants respectively (hereafter fixed to $J_{\mathrm{C}} = 10$ and $J_{\mathrm{Sh}} = -0.5 J_{\mathrm{C}}$). The

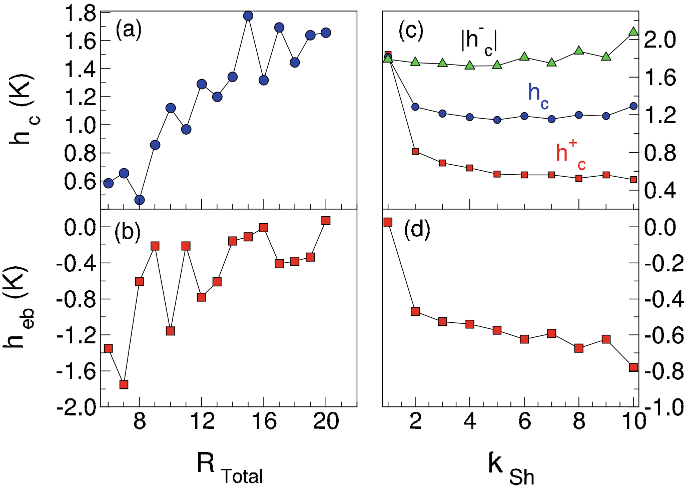

Fig. 1.21 Coercive and exchange bias fields for a spherical particle with $R = 12$, $R_{Sh} = 3$ and $k_C = 1$. The dependence on the particle radius is shown in panels (**a**) and (**b**), while in panels (**c**) and (**d**) the surface anisotropy k_{Sh} dependence is shown. Coercive fields at the decreasing and increasing field branches h_c^-, h_c^+ are also displayed in (**c**)

coupling at the interface is represented by $J_{\rm Int}$, that can be varied in sign and value to study the role played by the coupling across the core/shell interface on magnetic properties. Usually, $k_{\rm Sh} > k_{\rm C}$ is required in order for the shell spins not to reverse while cycling the magnetic field, so that EB is observed. Typically its value is higher than for the core due to reduced local coordination and will be fixed to $k_{\rm Sh} = 10$ K, in agreement with experiments [127, 128]. The core anisotropy will be fixed to $k_{\rm C} = 1$ K, which just sets the scale of the anisotropy field of the FM core.

Results of typical hysteresis loops obtained by MC simulation are shown in Fig. 1.20a for $J_{\rm Int} = -0.5 J_{\rm C}$, where the shift of the loop towards negative field values and a slightly increased coercivity for the loop after FC can be clearly seen. This can also be obtained for $J_{\rm Int} > 0$ [124]. In order to demonstrate that the origin of the loops shift is on the interface, we further computed the field dependence of the contribution of interface spins belonging to the shell, M_{Sh}^{Int}, to the total magnetization as displayed in Fig. 1.20b. The interfacial shell spins acquire a negative (or positive for AF coupling) net magnetization after FC which is higher than for the ZFC case [129], reflecting the fact that, after the FC process, a fraction of the interfacial spins are pinned and they remain so during the field reversal. In contrast, for the ZFC case, most of the interfacial spins follow the reversal of the FM core. The net magnetic moment, induced by the geometrical symmetry breaking and the alignment of groups of spins into the field direction, generates local fields on the core spins that point into the same direction as the external field, causing the shift of the hysteresis loops.

The results of the simulations allow us to understand that the origin of EB is a surface (interfacial) effect that, in contrast with those previously presented, scales with the number of uncompensated spins at the interface and not necessarily with the surface size. However, the peculiarities of the shape of the interface in a NM depend on its size and, as a consequence, EB is also affected by finite-size effects. As can be seen in panels (a) and (b) of Fig. 1.21, for increasing NP size, h_C also exhibits an increasing trend attributed to a higher proportion of interfacial core spins that have to be reversed. For h_{eb}, the tendency is the contrary, although with clear oscillations that are in complete correspondence to the ones observed in $M_{\rm int}$ attained after the FC process [125, 130]. This demonstrates again the direct link between the net magnetization component of the shell interfacial spins and the loop shifts. Finally, notice that surface anisotropy also influences all this phenomenology. As seen on panels (c) and (d) of Fig. 1.21, there is a minimal value of k_{Sh} for the observation of EB. On increasing k_{Sh} above it, the bias field increases progressively as the proportion of interfacial spins pinned during the hysteresis loop increases, and finally saturates. In contrast, in the presence of EB, h_C is reduced with respect to the low-anisotropy case, but its value does not show appreciable variations with k_{Sh}.

1.3.2.4 Effects of Surface Anisotropy on the Dynamics of NM

Availing ourselves of the compromise provided by the EOSP approach, i.e. a macrospin capturing some of the intrinsic features of the NM, we can then investigate the effects of surface anisotropy on the switching field. Accordingly, the relaxation rate turns out to be a non monotonic function of the surface anisotropy constant K_s [27]. More precisely, owing to the variation of the energy barrier as a function of the surface anisotropy (see Fig. 1.22 left), the relaxation rate increases for (small) increasing K_s (see Fig. 1.22 right) since the (surface) quartic contribution to anisotropy induces saddle points at the equator. As K_s further increases, the quartic anisotropy starts to dominate, inducing much deeper energy minima and thereby much higher energy barriers, which finally makes the switching less likely.

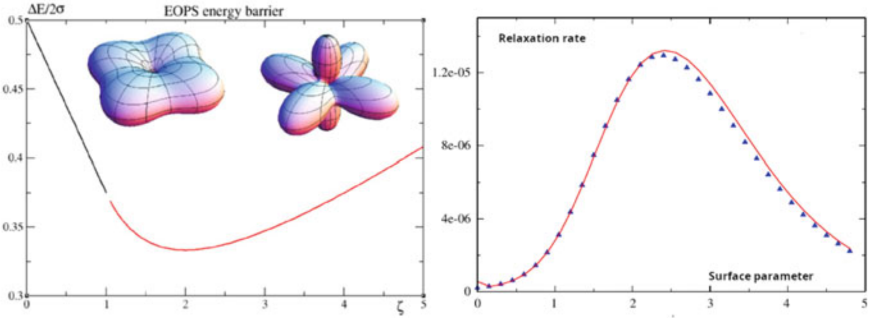

Fig. 1.22 Left: Energyscape with increasing surface anisotropy and the corresponding energy barrier. Right: Relaxation rate as a function of the surface parameter $\zeta = K_4/K_2$ (see (1.11)). *Source* Reprinted with permission from [1]. Copyright (2020), Elsevier Books

Compared to the effect of thermal fluctuations on the switching field, which is a simple scaling law, the effect of surface anisotropy depends on the direction of the applied field. This leads to a flattening of the switching field curve [27]. In the case of an assembly of magnetic NMs, this model is used to compute the ac susceptibility and to investigate the competition between (intrinsic) surface effects and dipolar interactions within an assembly of NM [28, 33–35].

1.3.2.5 Magnetic Excitations

When the conditions stated at the end of Sect. 1.2.2.2 regarding the limit of validity of the effective models are no longer satisfied, one has to adopt the full many-spin approach discussed earlier with the Hamiltonian in (1.7), and resort to fully numerical approaches, such as the Monte Carlo simulation method and/or the numerical solution of the Landau-Lifshitz equation, in order to study the equilibrium and dynamical properties of the NM. Among the results obtained for the equilibrium behavior, using the extended Monte Carlo approach that integrates both global and local spin rotations [2, 3], it has been shown that due to surface anisotropy the magnetization saturation requires relatively very strong magnetic fields ($\sim 10\,\mathrm{T}$). In addition, as was discussed earlier, the hysteresis loop exhibits various jumps which account for a (cluster-wise) switching of groups of atomic spins, and thus showing that the magnetization reversal is not a coherent mechanism as in the Stoner-Wohlfarth model. Regarding the many-spin approach to the magnetization reversal, it was shown in [131, 132] that, under specific conditions, second-generation spin waves can develop within the NM which, through their coupling to the uniform mode, destabilize the latter and ultimately induce the magnetization switching. More precisely, it was shown that a box-shaped NM exhibit an exponential spin-wave instability in the case of a uniaxial anisotropy and a linear spin-wave instability for a random anisotropy, with the exponential instability leading to a faster relaxation than the linear instability.

We have also studied surface effects on ferromagnetic resonance in magnetic nanocubes [133]. The numerical method used consists in linearizing the Landau-Lifshitz equation around the equilibrium state of the system, thus leading to an eigenvalue problem whose solution renders the excitation spectrum. For a box-shaped NM, the results were also compared to those of the generalized spin-wave theory [2, 3]. We computed the absorbed power as a function of the excitation frequency and showed that it is possible to attribute the different contributions of the surface and those of the core spins to the various peaks obtained by our calculations. In particular, the low-energy peak, corresponding to the $k = 0$ mode, consists of equal contributions from the surface and core spins. Furthermore, in the case of less symmetric box-shaped samples with Néel surface anisotropy, we observe an elliptic precession of the spins whose signature could be seen in a parametric resonance experiment. For 8 nm iron nanocubes, we show that the absorbed power spectrum should exhibit a low-energy peak around 10 GHz, typical of the uniform mode, followed by other low-energy features that couple to the uniform mode but with a stronger contribution from the surface. There are also high-frequency exchange-mode peaks around 60 GHz.

Finally, in the [134], the authors investigated the effects of surface anisotropy (and the ensuing spin misalignment) on the magnetization dynamics of ferromagnetic nanocubes in the many-spin approach. It was shown that such inhomogeneous spin configurations induce nutation in the dynamics of the particle's magnetization. In addition to the ordinary precessional motion with a frequency of 10 GHz, it was found that the dynamics of the net magnetic moment exhibits two more resonance peaks with frequencies that are higher than the FMR frequency. In particular, a much higher frequency of 1 THz was attributed to the magnetization fluctuations at the atomic level driven by exchange interactions.

1.4 Conclusion

In this chapter, we have studied the equilibrium, and to a lesser extent the dynamic, properties of nano-scaled magnetic systems taking account of their "intrinsic" features, such as finite-size, boundary and surface effects. We deemed it necessary to first emphasize the difference between these effects illustrated through simple models of a nanomagnet. Then, we presented the various models and approximations employed for describing nanomagnets depending on the range of their physical parameters and their ratios. Next, we discussed the corresponding computing methods that have been developed for these specific systems, such as the Monte Carlo simulations, Landau-Lifshitz equation (with and without the Langevin field), and the spin-wave theory.

We have covered some of our previous results for the thermal and hysteretic behavior of the magnetization. We first did so for model NM so as to build a qualitative picture of the general behavior and a fair understanding of the underlying mechanisms. Then, we considered more realistic NM with maghemite as the underlying structure as well as nanomagnets in core-shell configurations. For the model NM and the more realistic iron oxide nanocubes, we have also succinctly reported on some of our works that dealt with the effects of surface anisotropy on the relaxation rate and the spectrum of spin-wave excitations.

The examples studied allow us to appreciate the wealth of novel features and physical phenomena, and on the other hand the big challenges, brought about by nano-scaled spin systems. Their reduced size has deep consequences on their internal magnetic state as well as their macroscopic behavior. Indeed, finite-size, boundary and surface effects induce nonuniform magnetic states (spin noncolinearities) which lead to incoherent switching and novel hysteretic properties, reduced critical temperature and complex magnetization processes. The reduced size also leads to the interesting phenomenon of superparamagnetism which has redefined the relevant temperature and time scales. The study of the dynamics of such systems is a daunting task that requires the analysis of a multi-valley energy potential. Nevertheless, it has been possible to build macroscopic and microscopic models for investigating these phenomena and for shedding light on the underlying mechanisms. In addition, these models have allowed us to make estimates of the various physical parameters and to compare with experiments. It has thus been possible to figure out how the magnetization of the nanomagnet switches, to evaluate the corresponding relaxation time and the switching magnetic field. The macroscopic models such as the Stoner-Wohlfarth and Néel-Brown models have already been validated by experiments performed on nanomagnets for which these models are applicable. In the opposite situation induced by surface effects, we may say that only qualitative studies have been relatively successful, whereas any quantitative investigation still remains a challenge. However, the fast progress in synthesis, characterization and measurement has allowed for an unprecedented control of a whole set of properties of these nanomagnets and has made it to possible to shrink the gap between theory and experiments. In particular, the possibility of making well organised, nearly monodisperse assemblies of well defined nanomagnets, offers a real potential for studying the competition between, on one hand the intrinsic properties due to finite-size and boundary, shape and surface effects, and on the other the collective effects induced by mutual interactions between the nanomagnets and by their interactions with the hosting medium. This relatively favorable situation has triggered new impetus for further investigations of NMs assemblies with a plethora of promising practical applications.

Acknowledgements Ò.I. acknowledges financial support form the Spanish MINECO (No. MAT2015-68772 and No. PGC2018-097789-B-I00), Catalan DURSI (No. 2017SGR0598) and European Union FEDER Funds (una manera de hacer Europa), also CSUC for supercomputer facilities.

References

1. D.S. Schmool, H. Kachkachi, in *Single-Particle Phenomena in Magnetic Nanostructures* (Chap. 4), *Solid State Physics*, vol. 66, ed. by R.E. Camley, R.L. Stamps (Academic Press, 2015), pp. 301 – 423. https://doi.org/10.1016/bs.ssp.2015.06.001. http://www.sciencedirect.com/science/article/pii/S0081194715000053
2. H. Kachkachi, D.A. Garanin, Physica A **300**, 487 (2001). https://doi.org/10.1016/S0378-4371(01)00361-2
3. H. Kachkachi, D.A. Garanin, Euro. Phys. J. B **22**, 291 (2001). https://doi.org/10.1007/s100510170106
4. E.C. Stoner, E.P. Wohlfarth, Philos. Trans. R. Soc. London, Ser. A **240**, 599 (1948)
5. L. Néel, Compt. Rend. Acad. Sci. **228**, 664 (1949)
6. L. Néel, Compt. Rend. Acad. Sci. **237**, 1468 (1953)
7. W.F. Brown, Phys. Rev. **135**, 1677 (1963)
8. E.C. Stoner, E.P. Wohlfarth, IEEE Trans. Magn. **27**, 3475 (1991)
9. W.F. Brown, IEEE Trans. Magn. **15**, 1196 (1979)
10. A. Aharoni, *Introduction to the Theory of Ferromagnetism* (Oxford Science Pubs., 1996)
11. A. Aharoni, J. Appl. Phys. **83**, 3432 (1998). https://doi.org/10.1063/1.367113
12. J. Langer, Phys. Rev. Lett. **21**, 973 (1968)
13. J. Langer, Ann. Phys. (N.Y.) **54**, 258 (1969)
14. W.T. Coffey, D.A. Garanin, D.J. McCarthy, Adv. Chem. Phys. **117**, 483 (2001)
15. H. Kachkachi, J. Mol. Liquids **114**, 113 (2004)
16. T.L.S.I. Denisov, P. Hänggi, Phys. Rev. Lett. **97**, 227202 (2006)
17. G. Bertotti, I. Mayergoyz, C. Serpico, J. Appl. Phys. **91**, 7556 (2002)
18. Z.Z. Sun, X.R. Wang, Phys. Rev. B **74**, 132401 (2006)

19. C. Thirion, W. Wernsdorfer, D. Mailly, Nature Materials **2**, 524 (2003)
20. N. Barros, M. Rassam, H. Jirari, H. Kachkachi, Phys. Rev. B **83**, 144418 (2011)
21. N. Barros, M. Rassam, H. Kachkachi, Phys. Rev. B **88**, 014421 (2013)
22. H. Kachkachi, D.A. Garanin, in *Surface Effects in Magnetic Nanoparticles*, ed. by D. Fiorani (Springer, Berlin, 2005), p. 75
23. D.A. Garanin, H. Kachkachi, Phys. Rev. Lett. **90**, 065504 (2003). https://doi.org/10.1103/PhysRevLett.90.065504
24. H. Kachkachi, J. Magn. Magn. Mater. **316**, 248 (2007)
25. H. Kachkachi, E. Bonet, Phys. Rev. B **73**, 224402 (2006)
26. R. Yanes, O. Chubykalo-Fesenko, H. Kachkachi, D.A. Garanin, R. Evans, R.W. Chantrell, Phys. Rev. B **76**, 064416 (2007). https://doi.org/10.1103/PhysRevB.76.064416
27. Y. Kalmykov, P.-M. Déjardin, H. Kachkachi, J. Phys. D **41**, 134004 (2008)
28. F. Vernay, Z. Sabsabi, H. Kachkachi, Phys. Rev. B **90**, 094416 (2014)
29. S. Rohart, V. Repain, A. Thiaville, S. Rousset, Phys. Rev. B **76**, 104401 (2007)
30. R. Skomski, J.M.D. Coey, *Permanent Magnetism, Studies in Condensed Matter Physics*, vol. 1 (IOP Publishing, London, 1999)
31. K.B. Urquhart, B. Heinrich, J.F. Cochran, A.S. Arrott, K. Myrtle, J. Appl. Phys. **64**, 5334 (1988)
32. R. Perzynski, Yu.L. Raikher, in *Surface Effects in Magnetic Nanoparticles*, ed. by D. Fiorani (Springer, Berlin, 2005), p. 141
33. D. Ledue, R. Patte, H. Kachkachi, J. Nanosci. Nanotechnol. **12**, 4953 (2012)
34. G. Margaris, K. Trohidou, H. Kachkachi, Phys. Rev. B **85**, 024419 (2012)
35. Z. Sabsabi, F. Vernay, O. Iglesias, H. Kachkachi, Phys. Rev. B **88**, 104424 (2013). https://doi.org/10.1103/PhysRevB.88.104424
36. D.A. Dimitrov, G.M. Wysin, Phys. Rev. B **51**, 11947 (1995)
37. M. Dimian, H. Kachkachi, J. Appl. Phys. **91**, 7625 (2002)
38. K. Binder, D. Heermann, *Monte Carlo Simulation in Statistical Physics* (Springer, Berlin, 1992)
39. U. Nowak, R.W. Chantrell, E.C. Kennedy, Phys. Rev. Lett. **84**, 163 (2000). https://doi.org/10.1103/PhysRevLett.84.163
40. O. Chubykalo, U. Nowak, R. Smirnov-Rueda, M.A. Wongsam, R.W. Chantrell, J.M. Gonzalez, Phys. Rev. B **67**, 064422 (2003). https://doi.org/10.1103/PhysRevB.67.064422
41. U. Nowak, in *Annual Reviews of Computational Physics IX*, ed. by D. Stauffer (World Scientific, Singapore, 2001), chap. Thermally Activated Reversal in Magnetic Nanostructures, p. 105. https://doi.org/10.1142/9789812811578_0002
42. D. Hinzke, U. Nowak, Comp. Phys. Comm. **121–122**, 334 (1999). https://doi.org/10.1016/S0010-4655(99)00348-3
43. R.F.L. Evans, W.J. Fan, P. Chureemart, T.A. Ostler, M.O.A. Ellis, R.W. Chantrell, J. Phys.: Condens. Matter **26**, 103202 (2014). https://doi.org/10.1088/0953-8984/26/10/103202
44. D. Berkov, J. Magn. Magn. Mater. **186**, 199 (1998)
45. D.V. Berkov, N.L. Gorn, J. Phys.: Condens. Matter **13**, 9369 (2001)
46. S.V. Titov, H. Kachkachi, Y.P. Kalmykov, W.T. Coffey, Phys. Rev. B **72**, 134425 (2005). https://doi.org/10.1103/PhysRevB.72.134425
47. D.A. Dimitrov, G.M. Wysin, Phys. Rev. B **50**, 3077 (1994)
48. O. Iglesias, A. Labarta, Phys. Rev. B **63**, 184416 (2001). https://doi.org/10.1103/PhysRevB.63.184416
49. O. Iglesias, A. Labarta, F. Ritort, J. Appl. Phys. **89**, 7597 (2001)
50. R.H. Kodama, A.E. Berkowitz, E.J. McNiff, S. Foner, Phys. Rev. Lett. **77**, 394 (1996)
51. R.H. Kodama, S.A. Makhlouf, A.E. Berkowitz, Phys. Rev. Lett. **79**, 1393 (1997)
52. R.H. Kodama, A.E. Berkowitz, Phys. Rev. B **59**, 6321 (1999)
53. K. Binder, A.P. Young, Rev. Mod. Phys. **58**, 801 (1986)
54. H. Maletta, in *Excitations in Disordered Solids*, ed. by M. Thorpe (Plenum, New York, 1981)
55. H. Kachkachi, A. Ezzir, M. Noguès, E. Tronc, Surface effects in nanoparticles: Monte Carlo simulations. Eur. Phys. J. B **14**, 681 (2000)

56. H. Kachkachi, A. Ezzir, M. Nogués, E. Tronc, Eur. Phys. J. B **14**, 681 (2000)
57. D.P. Landau, Phys. Rev. B **14**, 255 (1976)
58. M.N. Barber, in *Phase Transitions and Critical Phenomena*, vol. 8, ed. by C. Domb, J.L. Lebowitz (Academic Press, New York, 1983), p. 145
59. H.E. Stanley, *Introduction to Phase Transitions and Critical Phenomena* (Oxford University Press, New York, 1987)
60. P.V. Hendriksen, S. Linderoth, P.-A. Lindgard, Phys. Rev. B **48**, 7259 (1993)
61. K. Binder, H. Rauch, V. Wildpaner, J. Phys. Chem. Sol. **31**, 391 (1970). https://doi.org/10.1016/0022-3697(70)90119-8
62. X. Obradors, A. Isalgue, A. Collomb, A. Labarta, M. Pernet, J.A. Pereda, J. Tejada, J.C. Joubert, J. Phys. C: Solid State Phys. **19**, 6605 (1986). https://doi.org/10.1088/0022-3719/19/33/010
63. J. Wang, W. Wu, F. Zhao, G.-m. Zhao, Appl. Phys. Lett. **98**, 083107 (2011). https://doi.org/10.1063/1.3558918
64. J. Wang, W. Wu, F. Zhao, G.-m. Zhao, Phys. Rev. B **84**, 174440 (2011). https://doi.org/10.1103/PhysRevB.84.174440
65. E. Skoropata, R.D. Desautels, B.W. Southern, J. van Lierop, Chem. Mater. **25**(9), 1998 (2013). https://doi.org/10.1021/cm303893h
66. L. Li, F.g. Li, J. Wang, G.m. Zhao, J. Appl. Phys. **116**(17), 174301 (2014). https://doi.org/10.1063/1.4900951
67. A.K. Pramanik, A. Banerjee, A. Banerjee, J. Phys.: Condens. Matter **28**(35), 35LT02 (2016). https://doi.org/10.1088/0953-8984/28/35/35lt02
68. X. Zhang, J. Wang, M. Gao, Mod. Phys. Lett. B **30**, 1650241 (2016). https://doi.org/10.1142/S0217984916502419
69. E. Velásquez, J. Mazo-Zuluaga, J. Restrepo, O. Iglesias, Phys. Rev. B **83**, 184432 (2011). https://doi.org/10.1103/PhysRevB.83.184432
70. E.A. Velásquez, J. Mazo-Zuluaga, D. Altbir, J. Mejía-López, Eur. Phys. J. B **87**, 61 (2014). https://doi.org/10.1140/epjb/e2014-40712-6
71. J. Alzate-Cardona, S. Ruta, R. Chantrell, O. Arbeláez-Echeverri, E. Restrepo-Parra, J. Magn. Magn. Mater. **424**, 451 (2017). https://doi.org/10.1016/j.jmmm.2016.10.108
72. E.S. Loscar, C.M. Horowitz, Phys. Rev. E **97**, 032103 (2018). https://doi.org/10.1103/PhysRevE.97.032103
73. B. Martínez, R.E. Camley, J. Phys.: Condens. Mat. **4**, 5001 (1992)
74. J.H. Park, E. Vescovo, H.J. Kim, C. Kwon, R. Ramesh, T. Venkatesan, Phys. Rev. Lett. **81**, 1953 (1998)
75. D. Zhao, F. Liu, D.L. Huber, M.G. Lagall, Phys. Rev. B **62**, 11316 (2000)
76. T. Hyeon, S.S. Lee, J. Park, Y. Chung, H.B. Na, J. Am. Chem. Soc. **123**, 12798 (2001). https://doi.org/10.1021/ja016812s
77. J. Park, K. An, Y. Hwang, J.G. Park, H.J. Noh, J.Y. Kim, J.H. Park, N.M. Hwang, T. Hyeon, Nat. Mater. **3**, 891 (2004). https://doi.org/10.1038/nmat1251
78. A. Labarta, X. Batlle, O. Iglesias, in *Surface Effects in Magnetic Nanoparticles*, ed. by D. Fiorani, Nanostructure Science and Technology (Springer, 2005), chap. From Finite-Size and Surface Effects to Glassy Behaviour in Ferrimagnetic Nanoparticles, pp. 105–140
79. L. Wu, A. Mendoza-Garcia, Q. Li, S. Sun, Chem. Rev. **116**, 10473 (2016). https://doi.org/10.1021/acs.chemrev.5b00687
80. A. Feld, A. Weimer, A. Kornowski, N. Winckelmans, J.P. Merkl, H. Kloust, R. Zierold, C. Schmidtke, T. Schotten, M. Riedner, S. Bals, H. Weller, ACS Nano **13**, 152 (2019). https://doi.org/10.1021/acsnano.8b05032
81. S. Tanaka, Y.V. Kaneti, N.L.W. Septiani, S.X. Dou, Y. Bando, M.S.A. Hossain, J. Kim, Y. Yamauchi, Small Methods **3**, 1800512 (2019). https://doi.org/10.1002/smtd.201800512
82. C. Martinez-Boubeta, K. Simeonidis, A. Makridis, M. Angelakeris, O. Iglesias, Sci. Rep. **3**, 1652 (2013). https://doi.org/10.1038/srep01652
83. P. Guardia, A. Riedinger, S. Nitti, G. Pugliese, S. Marras, A. Genovese, M.E. Materia, C. Lefevre, L. Manna, T. Pellegrino, J. Mater. Chem. B **2**, 4426 (2014). https://doi.org/10.1039/C4TB00061G

84. A.G. Kolhatkar, Y.T. Chen, P. Chinwangso, I. Nekrashevich, G.C. Dannangoda, A. Singh, A.C. Jamison, O. Zenasni, I.A. Rusakova, K.S. Martirosyan, D. Litvinov, S. Xu, R.C. Willson, T.R. Lee, ACS Omega **2**, 8010 (2017). https://doi.org/10.1021/acsomega.7b01312
85. E. Natividad, I. Andreu, in *Magnetic Characterization Techniques for Nanomaterials*, ed. by C.S. Kumar (Springer, Berlin, 2017), pp. 261–303. https://doi.org/10.1007/978-3-662-52780-1_8
86. Z. Nemati, J. Alonso, I. Rodrigo, R. Das, E. Garaio, J.Á. García, I. Orue, M.H. Phan, H. Srikanth, J. Phys. Chem. C **122**, 2367 (2018). https://doi.org/10.1021/acs.jpcc.7b10528
87. A.G. Roca, L. Gutiérrez, H. Gavilán, M.E.F. Brollo, S. Veintemillas-Verdaguer, M. del Puerto Morales, Advanced Drug Delivery Reviews **138**, 68 (2019). https://doi.org/10.1016/j.addr.2018.12.008
88. O. Iglesias, A. Labarta, Phys. Status Solidi C **1**, 3481 (2004). https://doi.org/10.1002/pssc.200405485
89. O. Iglesias, A. Labarta, J. Magn. Magn. Mater. **290–291**, 738 (2005). https://doi.org/10.1016/j.jmmm.2004.11.358
90. B. Martínez, X. Obradors, L. Balcells, A. Rouanet, C. Monty, Phys. Rev. Lett. **80**, 181 (1998)
91. Animated snapshots of the configurations along the hysteresis loops can be found at the web site: http://www.ffn.ub.es/oscar/SCM2004/SCM2004.html
92. S. Krupricka, K. Zaveta, in *Magnetic Oxides*, ed. by D.J. Craik (Wiley-Interscience, New York, 1975)
93. J.K. Vassiliou, V. Mehrotra, M.W. Russell, E.P. Giannelis, R.D. McMichael, R.D. Shull, R.F. Ziolo, J. Appl. Phys. **73**, 5109 (1993)
94. J.L. Dormann, F. D'Orazio, F. Lucari, E. Tronc, P. Prené, J.P. Jolivet, D. Fiorani, R. Cherkaoui, M. Nogués, Phys. Rev. B **53**, 14291 (1996)
95. F. Gazeau, E. Dubois, M. Hennion, R. Perzynski, Y.L. Raikher, Euro. Phys. Lett. **40**, 575 (1997)
96. O. Iglesias, A. Labarta, Phys. Rev. B **63**, 184416 (2001)
97. R.N. Bhowmik, R. Nagarajan, R. Ranganathan, Phys. Rev. B **69**, 054430 (2004). https://doi.org/10.1103/PhysRevB.69.054430
98. O. Iglesias, A. Labarta, Physica B **343** (2004). https://doi.org/10.1016/j.physb.2003.08.109
99. P.V. Hendriksen, S. Linderoth, P.-A. Lindgard, J. Phys.: Condens. Matter **5**, 5675 (1993)
100. O. Iglesias, A. Labarta, Physica B **343**, 286 (2004)
101. J. Restrepo, Y. Labaye, L. Berger, J.M. Greneche, J. Magn. Magn. Mater. **272–276**, 681 (2004). https://doi.org/10.1016/j.jmmm.2003.12.719
102. J. Mazo-Zuluaga, J. Restrepo, F. Muñoz, J. Mejía-López, J. Appl. Phys. **105**, 123907 (2009). https://doi.org/10.1063/1.3148865
103. Y. Labaye, O. Crisan, L. Berger, J.M. Greneche, J.M.D. Coey, J. Appl. Phys. **91**, 8715 (2002). https://doi.org/10.1063/1.1456419
104. L. Berger, Y. Labaye, M. Tamine, J.M.D. Coey, Phys. Rev. B **77**(10), 104431 (2008). https://doi.org/10.1103/PhysRevB.77.104431
105. J.Z. Jiang, G.F. Goya, H.R. Rechenberg, J. Phys.: Condens. Matter **11**, 4063 (1999)
106. E. Tronc, D. Fiorani, M. Nogués, A.M. Testa, F. Lucari, F. D'Orazio, J.M. Grenèche, W. Wernsdorfer, N. Galvez, C. Chenéac, D. Mally, J. Jolivet, J. Magn. Magn. Mater. **262**, 6 (2003)
107. Animated snapshots of the configurations along the hysteresis loops can be found at the web site: http://www.ffn.ub.es/oscar/HMM2003/HMMM2003.html
108. H. Kachkachi, M. Dimian, Phys. Rev. B **66**, 174419 (2002). https://doi.org/10.1103/PhysRevB.66.174419
109. M.P. Morales, S. Veintesmillas-Verdaguer, M.I. Montero, C.J. Serna, A. Roig, L. Casas, B. Martínez, F. Sandiumenge, Chem. Mater. **11**, 3058 (1999)
110. S.h. Noh, W. Na, J.t. Jang, J.H. Lee, E.J. Lee, S.H. Moon, Y. Lim, J.S. Shin, J. Cheon, Nano Lett. **12**, 3716 (2012). https://doi.org/10.1021/nl301499u
111. S.K. Sharma (ed.), *Exchange Bias: From Thin Film to Nanogranular and Bulk Systems* (CRC Press, 2017). https://doi.org/10.1201/9781351228459

112. M.A. Willard, L.K. Kurihara, E.E. Carpenter, S. Calvin, V.G. Harris, Int. Mater. Rev. **49**, 125 (2004)
113. S.B. Darling, S.D. Bader, J. Mater. Chem. **5**, 4189 (2005)
114. Q.A. Pankhurst, J. Connolly, S.K. Jones, J. Dobson, J. Phys. D **36**, R167 (2003)
115. P. Tartaj, M.P. Morales, T. González-Carreño, S. Veintemillas-Verdaguer, C. Serna, J. Magn. Magn. Matter **290–291**, 28 (2005)
116. K.M. Krishnan, A.B. Pakhomov, Y. Bao, P. Blomqvist, Y. Chun, M. Gonzales, K. Griffin, X. Ji, B.K. Roberts, J. Mater. Sci. **793**, 793 (2006)
117. J. Nogués, I.K. Schuller, J. Magn. Magn. Matter **192**, 203 (1999)
118. A.E. Berkowitz, K. Takano, J. Magn. Magn. Matter **200**, 552 (1999)
119. J. Nogués, J. Sort, V. Langlais, V. Skumryev, S. Suriñach, J. Muñoz, M. Baró, Phys. Rep. **422**, 65 (2005)
120. G. Salazar-Alvarez, J. Sort, S. Suriñach, M.D. Baró, J. Nogués, J. Am. Chem. Soc. **129**, 9102 (2007). https://doi.org/10.1021/ja0714282
121. O. Iglesias, A. Labarta, X. Batlle, J. Nanosci. Nanotechnol. **8**, 2761 (2008)
122. A.E. Berkowitz, G.F. Rodriguez, J.I. Hong, K. An, T. Hyeon, N. Agarwal, D.J. Smith, E.E. Fullerton, Phys. Rev. B **77**, 024403 (2008). https://doi.org/10.1103/PhysRevB.77.024403
123. A. López-Ortega, M. Estrader, G. Salazar-Alvarez, A.G. Roca, J. Nogués, Phys. Rep. **553**, 1 (2015). https://doi.org/10.1016/j.physrep.2014.09.007
124. O. Iglesias, X. Batlle, A. Labarta, Phys. Rev. B **72**, 212401 (2005). https://doi.org/10.1103/PhysRevB.72.212401
125. Ò. Iglesias, X. Batlle, A. Labarta, J. Phys. D **41**, 134010 (2008). https://doi.org/10.1088/0022-3727/41/13/134010
126. M.H. Phan, J. Alonso, H. Khurshid, P. Lampen-Kelley, S. Chandra, K. Stojak Repa, Z. Nemati, R. Das, Ó. Iglesias, H. Srikanth, Nanomaterials **6**, 221 (2016). https://doi.org/10.3390/nano6110221
127. E. Tronc, D. Fiorani, M. Nogués, A.M. Testa, F. Lucari, F. D'Orazio, J.M. Grenéche, W. Wernsdorfer, N. Galvez, C. Chanéac, D. Mailly, J.P. Jolivet, J. Magn. Magn. Mater. **262**, 6 (2003)
128. M.P. Morales, S. Veintemillas-Verdaguer, M.I. Montero, C.J. Serna, A. Roig, L. Casas, B. Martínez, F. Sandiumenge, Chem. Mater. **11**, 3058 (1999)
129. O. Iglesias, A. Labarta, Phys. B **372**, 247 (2006). https://doi.org/10.1016/j.physb.2005.10.059
130. D. De, O. Iglesias, S. Majumdar, S. Giri, Phys. Rev. B **94**, 184410 (2016). https://doi.org/10.1103/PhysRevB.94.184410
131. H.K.D.A. Garanin, L. Reynaud, Europhys. Lett. **82**, 17007 (2008)
132. D.A. Garanin, H. Kachkachi, Phys. Rev. B **80**, 014420 (2009)
133. R. Bastardis, F. Vernay, D.A. Garanin, H. Kachkachi, J. Phys. C: Condens. Matter **29**, 025801 (2017)
134. R. Bastardis, F. Vernay, H. Kachkachi, Phys. Rev. B **98**, 165444 (2018). https://doi.org/10.1103/PhysRevB.98.165444